Journal of African Earth Sciences 213 (2024) 105212

Contents lists available at ScienceDirect

Journal of African Earth Sciences

journal homepage: www.elsevier.com/locate/jafrearsci

Late Ediacaran post–collisional granite in Babouri–Figuil (Northwest Cameroon): Implication for crustal–mantle contributions in an extensional setting

Basua Afanga Archelaus Emmanuel [a,b,*], Changqian Ma [b], Kanouo Sylvestre Nguo [c], Lian-Xun Wang [b], David R. Lentz [d], Soumyajit Mukherjee [e], Bovari Yomeun Syprien [b], Yu-Xiang Zhu [b], Nformidah Ndah Siggy Signe [f]

[a] Department of Geology, University of Buea, P.O. Box 63, Buea, Cameroon
[b] School of Earth Sciences, China University of Geosciences, 430074 Wuhan, People's Republic of China
[c] National Advanced School of Mines and Petroleum Industries, Department of Mining Engineering and Mineral Processing, 08 Kaélé, Far North Region, Cameroon
[d] Department of Earth Sciences, University of New Brunswick, Fredericton, NB, Canada
[e] Department of Earth Sciences, Indian Institute of Technology Bombay, Powai, Mumbai-400 076, Maharashtra, India
[f] Institut fur Geologie, Universitat Bern, Baltzerstrase 1 + 3, Switzerland

ARTICLE INFO

Handling Editor: Dr Mohamed Mohamed G Abdelsalam

Keywords:
Northwest Cameroon domain
Neoproterozoic
Post–collisional granites
Mafic crustal protolith
Saharan metacraton

ABSTRACT

The Babouri–Figuil Magmatic Complex (BFMC, adjacent to the central-south Chad domain) is located on the southern flank of the Saharan Metacraton. It is amongst the least geologically studied regions in Cameroon; only a few key research papers on geochronology and isotopes have been completed. The emplacement of granitic bodies is poorly constrained between the early and late–Neoproterozoic with inherited zircons of older Paleoproterozoic–Neoproterozoic ages. In this study, undeformed biotite granite massifs (Lombel and Badesi) were studied, and their geochronologic, geochemical and mineral chemical data, including Nd–Sr–Hf isotopes, are presented. The massifs are enriched in pink K-feldspar (orthoclase and microcline; 60–65 wt%) and plagioclase (8–10 wt%) anastomosing to intergranular quartz (18–20 wt%) and biotite (3–5 wt%) crystals. The Lombel massif yielded a Concordia age of 566 ± 2.5 Ma (MSWD = 1.6, zircon U–Pb), slightly older than the Concordia age of 556 ± 2.7 Ma (MSWD = 2.1, zircon U–Pb) obtained for the Badesi massif. These are interpreted as emplacement ages, which post–date arc magmatism by ~ 45 Ma. The geochemistry of the massifs showed sub- to mid–alkaline, high–K alkali–calcic, and weakly peraluminous compositional characteristics. The calculated biotite temperatures ranged from 613 to 647 °C, pressures from 100 to 300 MPa, and H_2O from 3.0 to 3.5 wt%. Whole–rock composition geothermobarometry revealed low pressure of 100–500 MPa, depths of 3.5–18 km and low oxygen fugacity (ΔQFM = −0.6), indicating reducing crystallization conditions. The estimated radiogenic isotopic values are similar for both massifs, falling in the range from initial $\varepsilon_{Hf}(t)$ = +2.6 to +8.4 and initial $\varepsilon_{Nd}(t)$ = +1.3 to +2.1, with a corresponding average initial Sr of 0.70212–0.70458. These radiogenic isotope values suggest a mantle–derived origin for this granite or the melting of a juvenile mafic crustal protolith, as confirmed by the two–stage model age obtained (TDM_2 = ~ 1.2 Ga). Given that biotite is interstitial in alkali feldspar and plagioclase in both massifs, this suggests that biotite chemistry records conditions of magma evolution. Overall, these results confirm that the studied massifs are post–collisional products emplaced at shallow crustal levels under evolved magmatic conditions. They are coeval with a few post–magmatic intrusions in the central–south Chad and emplaced after the Sao–Francisco Congo Craton collided with the Saharan Metacraton. The ages obtained enabled a possible correlation with several Neoproterozoic post–collisional granites in Cameroon, south-central Chad, Central African Republic and Borborema Province of Brazil. The ages also revealed that continental assembly coupled with regional late–magmatism occurred during the Proterozoic.

* Corresponding author. Department of Geology University of Buea P.O Box 63, Buea, Southwest Region, C, Cameroon/o Faculty of Sciences, University of Buea, Switzerland.
E-mail address: basfanga@yahoo.com (B.A. Archelaus Emmanuel).

https://doi.org/10.1016/j.jafrearsci.2024.105212
Received 25 October 2023; Received in revised form 24 February 2024; Accepted 24 February 2024
Available online 7 March 2024

1. Introduction

The geologic events of the Proterozoic Eon were important in Earth's history and were characterized by major orogenic cycles and prolific granitic plutonism around continental arcs. Petrogenetic studies of these rocks provide windows to understand the evolution of the continental crust (e.g., Kemp and Hawkesworth, 2003; Frost et al., 2021), cratonic landmasses, and orogenic belts, such as those associated with continental Africa (Figs. 1 and 2a).

Africa, with territorial boundaries of ~ 30.37 million km^2, consists of cratonic complexes sandwiched by orogenic belts (e.g., Kennedy, 1964; Kroner, 2004). The Central Africa Orogenic Belt (CAOB) separates the Saharan Metacraton and the Sao-Francisco Congo Craton to the north and south, respectively. To the west is the Tuareg–Nigeria complex, which in turn abuts against the West African complex, and to the east is the Arabian–Nubian complex (Figs. 1 and 2a). These cratonic complexes are dominantly Archean–Paleoproterozoic (e.g., Kennedy, 1964; Kroner, 2004). However, the Saharan Metacraton and Arabian–Nubian complex are covered by Sahara sand and sediments hosting patches of older rocks (Abdelsalam et al., 2002). As per Kennedy (1964), Kroner (1977), Abdelsalam et al. (2002), and Begg et al. (2009), the Sahara Metacraton suffered rejuvenation or reactivation of its older cratonic lithosphere that caused it to lose its cratonic signatures presumably by the Pan-African collision.

The central Sahara, which is geographically defined as the central part of the Sahara Metacraton, constitutes approximately three-fourths of Chad, a part of the North Africa Shield, and extends southward to the northern Cameroon domain (Figs. 1 and 2a). Because of limited studies, the tectono-magmatic evolution of the central Sahara remains enigmatic (Begg et al., 2009, Figs. 1 and 2a, b). For example, a few Precambrian massifs studied in central-south Chad and northern Cameroon (e.g., Penaye et al., 2006; Shellnutt et al., 2017, 2020) have not yet been clarified whether they belong to the Saharan Metacraton or to the CAOB (e.g., Djerossem et al., 2020).

According to geochronologic data from central-south Chad to north Cameroon (central Sahara), magmatic activity in these regions presumably occurred from ~ 1000 to < 570 Ma. Penaye et al. (2006) defined at least three major magmatic episodes. The first occurred as pre-collision mafic to intermediate complexes between 737 and 723 Ma, followed by the emplacement of syn–collisional, calc–alkaline granitic batholiths (665–638 Ma; e.g., Mayo–Kebbi in SW Chad). The final phase was the emplacement of post-collision granitoids (< 570 Ma, mostly alkaline in composition), followed by Cretaceous mafic dykes (Ngounouno et al., 2001). Based on combined zircon U–Pb and Rb–Sr whole–rock ages and tracer Sr–Nd–Hf radiogenic isotopes, it has been shown that these plutons were emplaced predominantly into Neoproterozoic crust (e.g., Penaye et al., 2006; Isseini et al., 2012; Shellnutt et al., 2017, 2018, 2020, 2021; Basua, 2021). A few Sr, Nd, and Hf isotopic data from granitoids alongside mafic to intermediate rocks suggest that the origin of most formations in central Sahara is the mantle (Penaye et al., 2006). This mantle source may reflect a magmatic arc that occurred in SW Chad to north Cameroon at ~ 750 Ma. A–type granites (A1 and A2; Eby, 1992) are amongst the studied calc–alkaline granitoids of this region in the central Sahara (e.g., Isseini et al., 2012; Shellnutt et al., 2018; Pham, 2018). In Figuil, the reported A–type granites revealed at least three magmatic episodes at ~ 707, ~ 600, and < 570 Ma, respectively, using U–Pb zircon dating (Basua, 2021; Basua et al., 2022). These ages conform to those reported in the literature (e.g., Penaye et al., 2006; Isseini et al., 2012; Dawaï et al., 2013; Shellnutt et al., 2018). Sr–Nd isotopes have been used to constrain the petrogenesis of these granites (e.g., Isseini et al., 2012; Pham, 2018; Shellnutt et al., 2018). In addition, Basua (2021) and Basua et al. (2022) applied Sr–Nd–Hf tracer isotope techniques to better constrain the source rock for the A–type granites that are exposed at Figuil in northern Cameroon (Fig. 2b–d). The results indicate regional magmatism in Cameroon, Chad, and the Central Africa Republic and a mantle-derived origin or the existence of a mafic residual crust within the southern limit of the Sahara Metacraton (e.g., Isseini et al., 2012; Shellnutt et al., 2018; Basua et al., 2022). The Sr–Nd–Hf tracer isotopic data reflects the variable degree of late crystallization of a mafic melt.

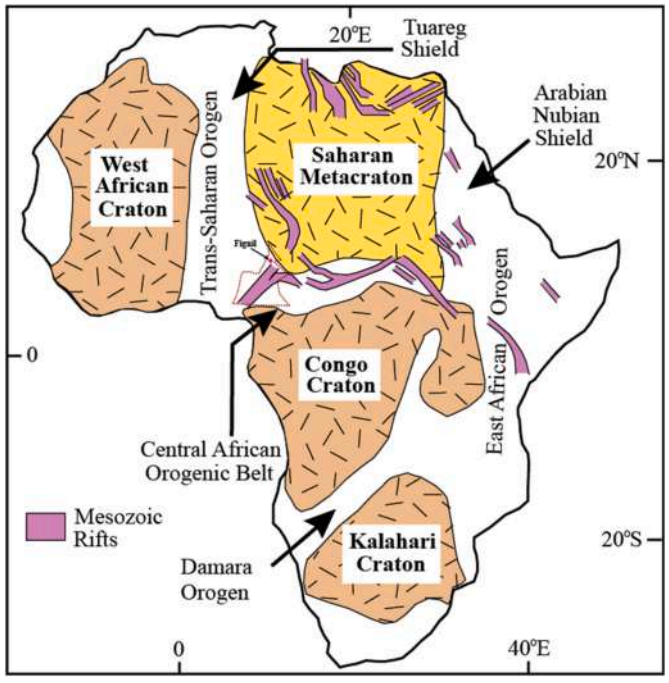

Fig. 1. Sketch map of Africa showing the distribution of Precambrian cratons, metacratons, and Mesozoic orogenic belts (modified from Abdelsalam et al., 2011).

Data on Ediacaran post–collisional A–type granites of ages < 570 Ma studied in SW Chad are unavailable for the Cameroon domain. Because these ages probably mark the end of the Pan-Africa orogeny, whether SW Chad experienced a distinct and prolong orogeny relative to Cameroon remains indeterminate. A progressive tectonic evolution between these two adjacent domains can be better described if the petrogenesis of the outcropping rocks is reviewed using a robust dataset.

In this article, we use petrography, major and trace element geochemistry, U–Pb zircon geochronology, Hf–Sr–Nd tracer isotopic analyses, and biotite compositional analysis to characterize and classify the Neoproterozoic post-collisional A–type granite of the Babouri–Figuil Magmatic Complex (BFMC). The results were also used to determine the nature and source of these granites, the timing of tectono–magmatic evolution, the condition of generation, and to characterize post–emplacement events.

2. Geologic background

The Central Africa Orogenic Belt (CAOB; in Cameroon, Chad, and Central Africa Republic; Figs. 1 and 2a) consists of structurally–related Archean to Proterozoic domains that were remobilized in the Neoproterozoic during the Pan–African orogeny (e.g., Abdelsalam et al., 2002). Its formation is usually linked to the continental–continental collision between the West African Craton, Congo Craton, and Sahara Metacraton (Abdelsalam et al., 2002; Toteu et al., 2004; Penaye et al., 2006; Ngako et al., 2008) (Figs. 1 and 2a). In Cameroon, the CAOB is divided into at least three geotectonic domains separated by major fault zones (e.g., Toteu et al., 2004; Ngako et al., 2008) (Fig. 2a and b). These are the southern block (Yaounde domain), central block (Adamawa–Yade domain), and northern block (NW Cameroon domain) (e.g., Toteu et al., 2004; Ngako et al., 2008; Fig. 2b).

The southern domain is located south of the central Cameroon shear zone (CCSZ); it is largely represented by the Yaounde Group, which is

limited to the north and south by the Sanaga Shear Zone and Congo Craton, respectively. It extends to the Central Africa Republic and consists of various igneous lithologies, such as mafic to intermediate rocks (pyroclastics), rare late-post granitoids, and serpentinized ultramafic rocks rich in Cr and Ni (e.g., Vicat et al., 1997), as well as inculcated metasedimentary rocks. The central domain is limited to the north by the Tchollire–Banyo Shear Zone (TBSZ) (Fig. 2b) and consists of large remnants of Paleoproterozoic metasedimentary rock and orthogneisses, Cretaceous acid volcaniclastic rocks, and syn- to late-tectonic Pan–African granitoids (e.g., Toteu et al., 2001; Kamani et al., 2021; Ngatcha et al., 2022; Yomeun et al., 2022a,b). The northern domain is located west of the TBSZ (Fig. 2b). It is composed of metamorphic rocks (schists, metabasites, and gneisses) attributed to medium- to high–grade Neoproterozoic metamorphism related to a volcanic protolith (e.g., Toteu, 1990). Tholeiitic basalts, calc–alkaline rhyolites of ~ 800 Ma, and pre- to post–tectonic granitoids have also been found (e.g., Toteu et al., 2001).

The study area of Figuil is in the northern Cameroon domain and is adjacent to the SW Chad domain (Fig. 2b). According to Toteu (1990) and Penaye et al. (2006), these domains belong to an early Neoproterozoic back-arc basin and represent the southern limit of the Saharan Metacraton (Shellnutt et al., 2015; Basua et al., 2022). To the NE of Figuil is the Mayo-Kebbi batholith in SW Chad (Isseini et al., 2012). To the south is the Poli Group (Fig. 2b), and to the west is the eastern Nigerian block (Fig. 2a). This zone presumably resulted from successive tectonic collages of the NW Cameroon, Mayo–Kebbi, and Adamaw–Yade domains at < 620 Ma (Penaye et al., 2006). This collisional–assemblage initiated magmatism in the NW Cameroon domain (Toteu et al., 2001). For instance, widespread migmatisation occurred after the E–W collision < 612 Ma (Penaye et al., 2006). Moreover, post–tectonic granitoids emplaced at ~ 600 Ma confirmed that they postdated the final tectonic collage (Penaye et al., 2006). Associated deformations, such as the D_2 phase, were fingerprinted in a metadiorite that yielded ~ 612 Ma of the Poli Group (Fig. 2b). It is considered the maximum age of D_2 regional foliation within the Cameroon Formation (Toteu et al., 2004). Mafic to intermediate plutons southwards of the

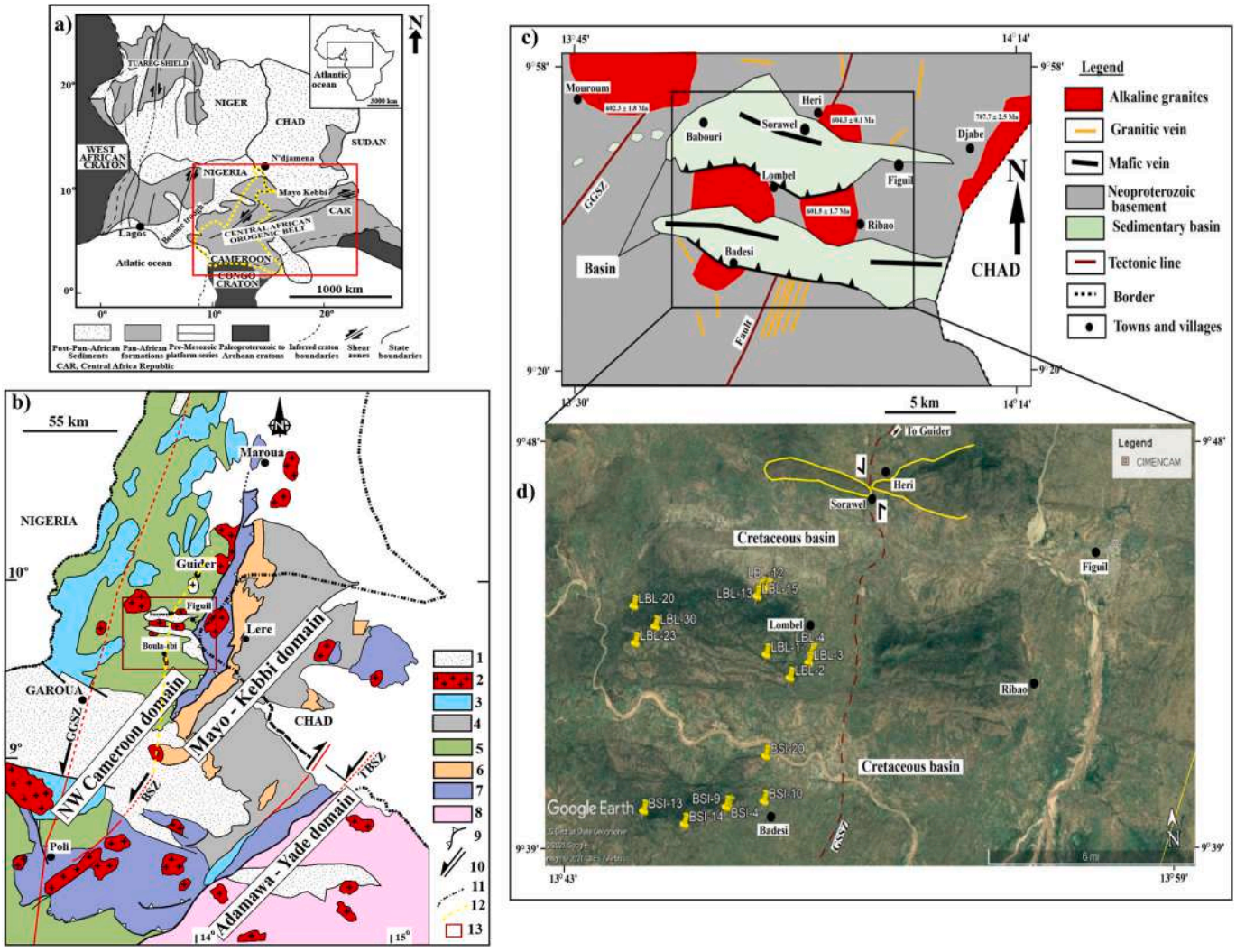

Fig. 2. Geologic map locating the study area in the regional setting. (a) Map of central and west-African orogenic belts. Red rectangle: locating Cameroon in central Africa; (b) geologic map of NW Cameroon showing location of study area (modified after Penaye et al., 2006): *(1)* post- Pan–African sediments, *(2)* late– to post-tectonic Pan–African granitoids, *(3)* syntectonic granite, *(4)* Mayo Kebbi batholiths: tonalite, trondhjemite and granodiorite, *(5)* medium- to high-grade gneisses of the West Cameroon domain, *(6)* mafic to intermediate complex of the Mayo Kebbi region (metadiorite and gabbro-diorite) and amphibolites, *(7)* Neoproterozoic late- to medium-grade volcano-sedimentary sequence: Zalbi, Gouegoudoum and Poli groups, *(8)* remobilized paleoproterozoic Adamawa–Yade domain, *(9)* thrust front, *(10)* strike-slip faults, TBZ, Tchollire-Banyo Shear zone, GGSZ, Gode–Gormaya shear zone, *(11)* State border. *(12)* Speculative NE extension of the Balche shear zone (BSZ), *(13)* red rectangle indicates the study area; (c) Sketch geological map of the study area showing distribution of the studied (SW) and other massifs. (d) Sample locations on the studied massifs (Lombel and Badesi) positioned to the west of the N–S trending Guider–Sorawel Shear Zone (GSSZ), modified from the source map of Garoua–E drawn by Schwoerer (1962).

Poli Group yielded syn-D_1 deformation dates of ~ 633–620 Ma (Toteu et al., 1987).

A previous study in Figuil indicated that magmatism of the A–type granites started in the Early Neoproterozoic to Late Neoproterozoic and displayed at least three magmatic episodes of ~ 707, 600, and 566–555 Ma (zircon U/Pb age) (Basua, 2021). The older age connotes arc magmatism in this area, the middle age indicates syn–collisional to late–collisional granitoids, and the younger ages denote other post-–collisional granitoids in an extensional setting at the southern limit of the Saharan Metacraton (Basua et al., 2022). These granites, mostly the two younger groups, are undeformed, and their isotopic information matches such an evolution (e.g., Basua et al., 2022; Li et al., 2017). The obtained ages are consistent with the reported geochronologic data in nearby terrains found in Cameroon and Chad (Penaye et al., 2006; Isseini et al., 2012; Shellnutt et al., 2015, 2017, 2018; Li et al., 2017).

The Figuil granitoids are associated with tholeiitic dolerites, gabbros, olivine basalts (Basua, 2021), camptonites (Ngounouno et al., 2001), mica schists, chlorite schists, talc schists, marbles, and gneisses (Schwoerer, 1962; Toteu et al., 1987; Basua, 2021) all of unconstrained age. The basement rocks are affected by an E–W strike–slip fault that initiated formation of the Babouri–Figuil Cretaceous basin, probably related to extensional tectonics linked to the opening of the South Atlantic Ocean (Guiraud and Maurin, 1992) (Fig. 2c and d). Migmatites host numerous mafic and felsic dykes and dykelets representing

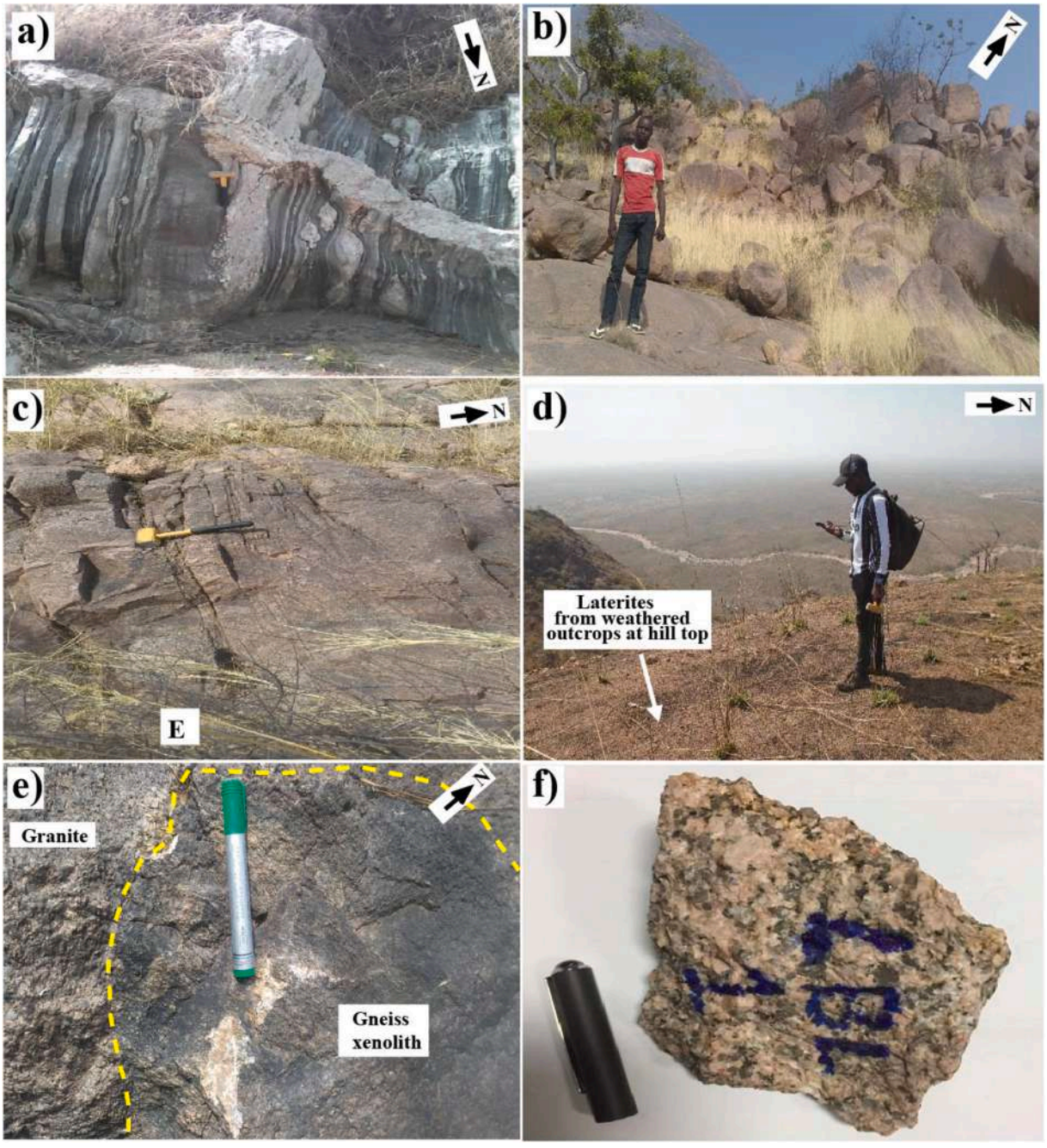

Fig. 3. Field photographs of the studied granite massifs: (a) vertical cross-section of leucocratic, mesocratic, and amphibolitic bands in gneiss along a river bed east of Figuil village; (b) side view of the Lombel massif showing dome and blocks; (c) West-East oriented shear bands on granite dome at the Lombel massif, E stands for East; (d) laterites from weathered outcrop at hill top west of the Lombel massif; (e) gneiss xenoliths in granite south from the Lombel village, (f) hand specimen reddish granite Lombel massif.

post–emplacement fracture-filling, indicating features probably formed during brittle events and partial fusion (Basua, 2021; Kanouo et al., 2021a). Metamorphic basement rocks and alkaline granitic intrusions are uncomfortably overlain by Cretaceous sandstones, marls, mudstones, shales, limestones, and Quaternary deposits (Schwoerer, 1962; Guiraud and Maurin, 1992; Kanouo et al., 2021a). Sedimentary rocks in the Babouri–Figuil area were affected by Cenozoic tectono–volcanism, giving rise to camptonites and trachytes that locally overlie sandstones (Schwoerer, 1962; Ngounouno et al., 2001).

3. Field & sample description

The studied plutons cropping out in the Lombel and Badesi massifs cut across the weakly to strongly banded migmatitic orthogneisses representing the basement rock of the Babouri–Figuil Magmatic Complex (Basua, 2021; Basua et al., 2022; Fig. 2b–d). These migmatites were deformed and re-equilibrated during the late Neoproterozoic. They are marked by N–S to NNE–SSW-trending steeply dipping foliations and tight–upright folds (Fig. 3a). These rocks show gradational and sharp contacts, aided by their distinct colors and components.

The Lombel and Badesi massifs (Basua, 2021) are made up of several plutons semi–circular in plan and can reach up to 800 m in height in some areas (Figs. 2d and 3 b-d). In the field, these plutons are indistinguishable (e.g., reddish when not altered and medium- to coarse–-grained textures) in the north and south of the W–E Babouri–Figuil Basin (Fig. 3c and d). Granitic outcrops of these plutons manifest as domes and boulders (> 3 m) and enclose felsic lenses and pockets (Fig. 3b). Late aplitic granitic and medium-grained to pegmatitic quartz veins are not uncommon within the plutons and are locally displaced sinistrally by W–E shear bands (Fig. 3c). Granite blocks at the top of a few massifs were weathered to laterite (Fig. 3d). Close to the border of some plutons (e.g., east of the Lombel Massif), pieces of gneisses are locally found in the studied granites (e,g., Fig. 3e). Near the contact zones, the rocks are incipiently foliated at the pluton margins, possibly owing to their mechanical interaction with the host during emplacement as a crystal-laden mush.

In hand specimens, the studied granites are composed predominantly of red feldspars, quartz grains, and biotites (Fig. 3f). Petrography reveals that these intrusive rocks have a coarse-grained to locally pegmatitic texture (Fig. 3f). Mineralogically, they are proportionally composed of alkali feldspars (60–65 vol%), quartz (18–20 vol%), plagioclase (8–10 vol%), and biotite (3–5 vol%) (Fig. 4). The alkali feldspars and plagioclase laths are similar in size. They are euhedral to subhedral and mostly

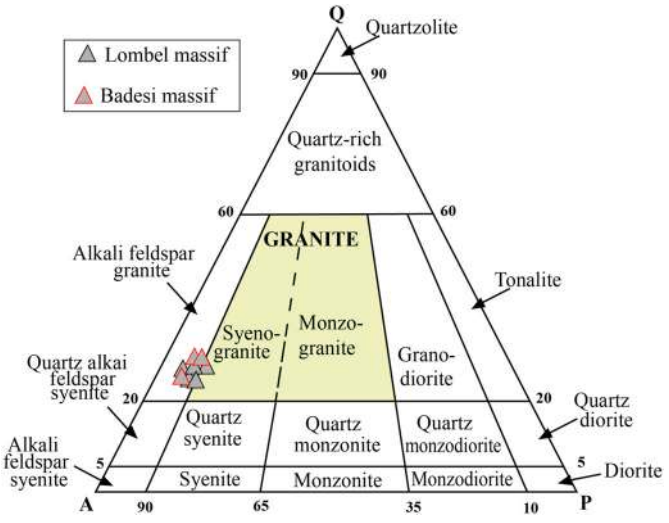

Fig. 4. Petrographic classification (QAP; Streckeisen, 1976) diagram of the granite from the Lombel and Badesi massifs.

occur in longitudinal sections in terms of megacrysts (> 2 cm long) and phenocrysts (< 1 cm long) (Fig. 5a and b). Feldspars display Carlsbad and microcline twinning, and only a few crystals are perthitic.

Plagioclase occurs in two generations: *(1)* as inclusions in feldspar and quartz (Fig. 5a) and *(2)* as large crystals close to alkali feldspar laths. Some plagioclase laths were zoned, whereas others showed surface alteration and local saussuritization. The quartz is anhedral with a few zircon inclusions (Fig. 5c). Quartz and alkali feldspar have consertal textures. Myrmekite occurs at the contact between plagioclase and orthoclase; a few sections display granophyric textures (Fig. 5d and e). Biotite flakes are euhedral to subhedral, and crystals host acicular apatites, which are euhedral and elongated to rounded along with zircon inclusions (Fig. 5f–h). In a few thin sections, biotite was altered to chlorite (Fig. 5i and j). Accessory mineral phases include euhedral apatite, zircon, titanite, and allanite (Fig. 5f–j). Chlorite, Fe–Ti oxides, and muscovite occur as secondary products (Fig. 5k). A few sections showed crushed minerals bound by micro-shear bands, indicating sinistral slip (Fig. 5l). From this assessment, one can infer that these massifs were locally tectonized and altered because biotite had turned to chlorite and plagioclase into saussaurite. Table 1 summarizes the normative mineral calculations by the Cross, Iddings, Pirsson, and Washington (CIPW) norm for the modal compositions of the samples from the Lombel and Badesi massifs.

4. Methods

The analytical methods were considered based on their high accuracy and reliability for characterizing granites. During fieldwork, over 60 samples were collected from both massifs. No specific differences in mineral composition or textural features were noted in macro- or microscopic studies. Sixteen biotite crystals selected from these massifs were analyzed for biotite chemical composition using the electron probe micro-analysis technique (EPMA) (Table 2). U–Pb zircon dating vis-à-vis *in situ* Lu–Hf isotopes at 40 spots was performed for a single sample from each intrusion (Tables 3 and 4). Three samples from the Badesi massif and five from the Lombel massif were analyzed for major- and trace–-element geochemistry using fusion Inductively Coupled Plasma–Mass Spectrometry (ICP–MS) (Table 5). Four samples from both massifs were analyzed for whole–rock Sr–Nd tracer radiogenic isotopes (Table 6). An automatic calculation worksheet of Zhang et al. (2003) for igneous acid rocks (granites) alongside eqn. (1) of Luhr et al. (1984) and eqn. (2) of Uchida et al. (2007) were used to estimate the biotite temperatures and pressures, respectively. A Microsoft Excel spreadsheet program by Yang et al. (2021) was applied to estimate the ferric-ferrous iron oxide ratio and granite crystallization temperatures, pressures, depths, and oxygen fugacity (Table 7). This entails the input of whole–rock analytical data of granitoids into certain cells (e.g., B4 and B19), as indicated in e-Table 1. Then, a number, for instance, −0.55, constrained by the Fe–Ti oxide mineral assemblage of the sample, was input into cell B3 to perform the calculation. This Microsoft Excel consists of four spreadsheets (e-Tables 1–4) by the formulae and equilibrium parameters used for conversion of ΔFQM to log (fO_2) values. For details, see the supplementary spreadsheet of Yang et al. (2021).

4.1. Biotite chemical analysis

The chemical composition of the biotite was determined using a JEOL JXA–8230 Electron Probe Microanalyzer (EPMA) equipped with five wavelength-dispersive spectrometers (WDS) at the Microscopy and Microanalysis Laboratory, Wuhan Microbeam Analysis Technology Co., Ltd. The samples were first coated with a thin conductive carbon film before analysis. The protocol suggested by Zhang et al. (2016) was used to minimize the difference in carbon film thickness between the samples and obtain a ca. 20 nm uniform coating. Detailed information is provided in the supplementary file of this article.

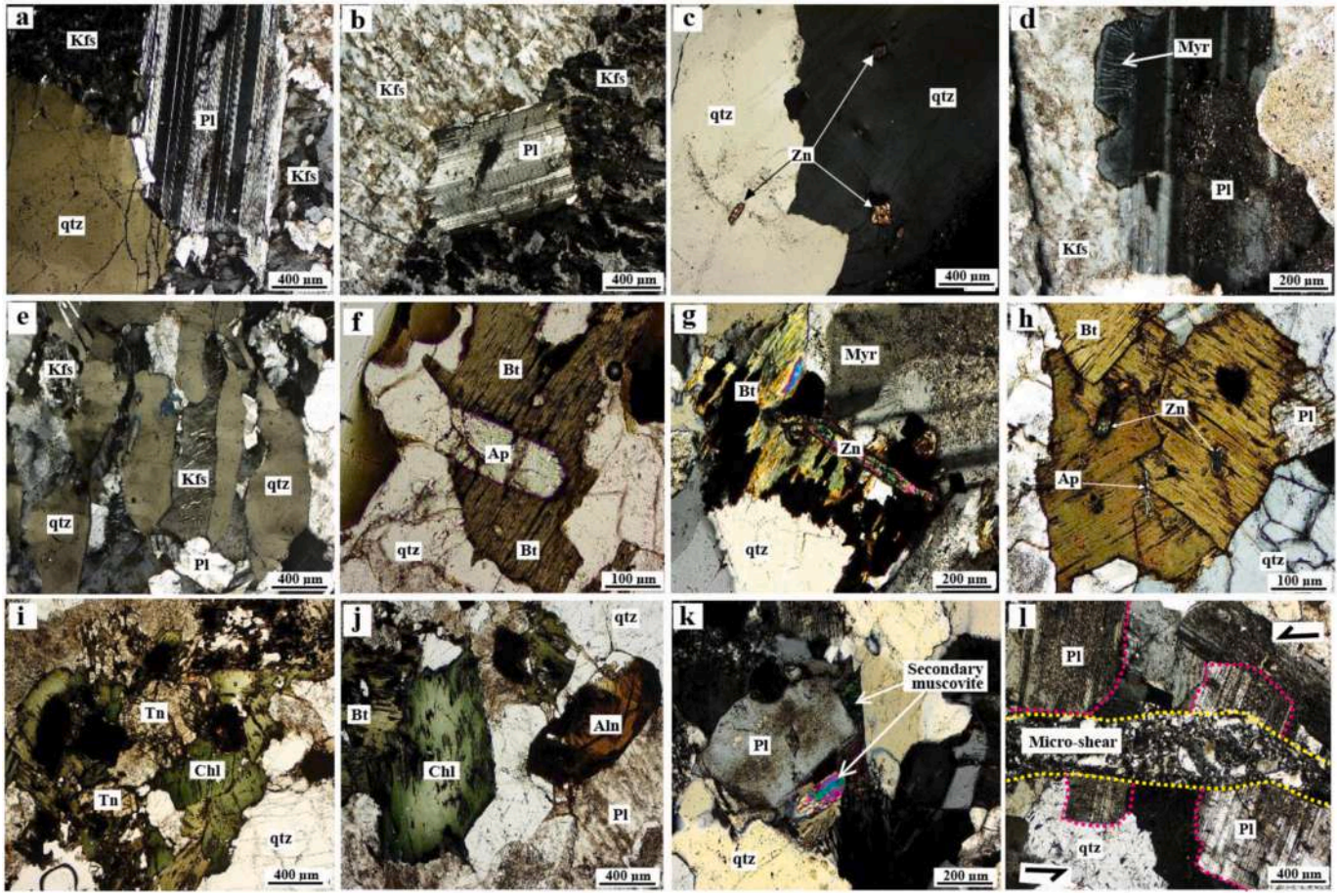

Fig. 5. Photographs of biotite granite from the Lombel and Badesi massifs, including principal minerals such as feldspar, plagioclase, quartz, biotite, and secondary mica (muscovite) found in fractures, photos taken under crossed polarized light: (a) Polysynthetic twinned plagioclase; (b) Carlsbad twin in K-feldspar hosting second generation plagioclase; (c) zircon inclusion in quartz; (d) Myrmekite between plagioclase and K-feldspar; (e) graphic - granophyric texture; (f–h) apatite and zircon inclusion in biotite; (i–j) association of titanite, allanite, chlorite, and Fe–Ti oxides; (k) secondary muscovite in interstitial spaces. (l) Microshear in granite indicating sinistral movement offractured plagioclase crystals. Kfs = feldspar, Pl = plagioclase, Qz = quartz, Bt = biotite, Chl = chlorite, Zn = zircon, Tn = titanite, Aln = allanite, Ap = apatite, and Myr = myrmekite.

Table 1
Normative mineral calculations by Cross, Iddings, Pirsson, and Washington (CIPW) norm modal compositions of the granite from the Lombel and Badesi massifs.

	Lombel					Badesi		
	LBL-1	GLBL-7	LBL-13	LBL-20	LBL-21	BSI-4	BSI-10	BSI-14
Q	33.14	32.33	42.10	34.38	30.76	33.70	25.65	32.70
C	0.51	0.36	1.52	0.31	0.54	0.34	0.13	0.37
Or	29.79	29.55	25.23	27.01	30.32	29.55	34.22	24.11
Ab	30.72	30.38	26.40	33.09	29.70	29.79	34.19	38.25
An	2.52	2.98	1.26	2.27	2.90	3.09	3.16	2.07
Hy	2.22	2.85	1.96	2.35	3.38	2.39	1.75	1.28
Mt	0.33	0.41	0.29	0.35	0.48	0.35	0.26	0.19
Il	0.19	0.29	0.19	0.13	0.42	0.23	0.13	0.04
Ap	0.02	0.07	0.05	0.02	0.12	0.05	0.02	0.02
Sum	99.43	99.21	99.01	99.90	98.61	99.49	99.50	99.03

4.2. Zircon U–Pb dating

The analyzed zircons were from the biotite granite that crops out at the Lombel and Badesi massifs. Zircon grains from ~ 2 kg of pulverized bulk rock samples was separated using a Wilfley table, Frantz isodynamic separation, and heavy liquids, and grains were picked under a binocular microscope at the Langfang Yuneng Rock Mineral Sorting Technology Service Co. Ltd. Only selected grains of the zircon population were observed under transmitted and reflected light using an optical microscope. Zircon Cathodoluminescence (CL) images were obtained using CAMECA SX51 at appropriate conditions of 50 kV and 15 nA at Wuhan Sample Solution Analytical Technology Co. Ltd., Wuhan (China). From the obtained CL images, potential points were selected for U–Pb dating and Lu–Hf isotopic analysis.

Simultaneous U–Pb dating, and zircon trace–element analysis were performed at Wuhan Sample Solution Analytical Technology Co. Ltd., Wuhan, China. The experiments were performed using an Agilent 7700e ICP-MS instrument (Agilent Technology, Tokyo, Japan) together with an excimer laser COMPexPro 102 ArF (wavelength of 193 nm and maximum energy of 200 mJ). Zong et al. (2017) presents other

Table 2
Biotite chemical composition for Lombel and Badesi biotite granite.

	Biotites from Lombel massif								Biotites from Badesi Massif							
	LBLT-bt1	LBLT-bt2	LBLT-bt3	LBLT-bt4	LBLT-bt5	LBLT-bt6	LBLT-bt7	LBLT-bt8	BSI-4-bt1	BSI-4-bt2	BSI-4-bt3	BSI-4-bt4	BSI-4-bt5	BSI-4-bt6	BSI-4-bt7	BSI-4-bt8
SiO_2	33.92	34.13.	33.81	34.35	34.07	33.33	34.57	34.70	33.89	33.86	34.63	34.44	34.34	34.42	34.74	35.02
TiO_2	3.29	3.45	2.89	3.07	3.60	3.18	3.19	3.10	3.73	3.59	3.69	3.48	3.73	3.60	3.58	3.77
Al_2O_3	13.44	14.07	14.56	14.16	13.26	13.28	14.03	14.23	12.29	12.53	12.32	12.36	12.59	12.07	12.24	12.45
FeOt	32.60	31.44	32.14	31.60	32.81	31.55	32.05	31.79	30.33	31.41	30.60	31.18	30.35	31.47	30.71	30.40
MnO	0.89	0.88	0.88	0.96	0.86	0.81	0.83	0.90	0.77	0.65	0.80	0.56	0.84	0.84	0.82	0.84
MgO	1.91	2.05	1.91	2.20	2.09	2.02	2.09	2.02	3.89	3.98	3.88	3.79	3.94	3.86	3.96	3.86
CaO	0.00	0.00	0.03.	0.07	0.02	0.05	0.00	0.05	0.22	0.02	0.00	0.00	0.07	0.08	0.09	0.07
Na_2O	0.16	0.07	0.06	0.09	0.13	0.12	0.10	0.10	0.07	0.04	0.06	0.08	0.08	0.11	0.11	0.07
K_2O	9.60	9.53	9.69	9.40	9.47	9.35	9.59	9.52	9.17	9.21	9.76	9.51	9.41	9.34	9.41	9.59
P_2O_5	0.00	0.03	0.00	0.03	0.00	0.00	0.02	0.05	0.02	0.00	0.00	0.00	0.03	0.00	0.00	0.00
Cr_2O_3	0.05	0.00	0.00	0.00	0.04	0.01	0.00	0.02	0.04	0.00	0.00	0.02	0.01	0.01	0.00	0.01
F	1.15	1.05	0.67	0.94	1.10	0.83	1.04	0.93	0.50	0.33	0.78	0.62	0.75	0.80	0.73	0.82
Cl	0.17	0.16	0.10	0.15	0.14	0.13	0.14	0.17	0.07	0.10	0.07	0.09	0.10	0.07	0.12	0.08
Total	96.66	96.38	96.42	96.58	97.09	94.28	97.18	97.14	94.75	95.58	96.25	95.85	95.91	96.31	96.16	96.61
FeO/(FeO + MgO)	0.94	0.93	0.94	0.94	0.94	0.94	0.93	0.94	0.88	0.88	0.89	0.89	0.88	0.89	0.88	0.88
FeO/MgO	17.10	15.34	16.85	14.35	15.67	15.63	15.32	15.74	7.79	7.90	7.89	8.22	7.69	8.16	7.75	7.87
apfu																
Si	5.62	5.60	5.54	5.61	5.61	5.61	5.63	5.63	5.59	5.54	5.66	5.64	5.62	5.64	5.67	5.68
AlIV	2.38	2.40	2.46	2.39	2.39	2.39	2.37	2.37	2.39	2.42	2.34	2.36	2.38	2.33	2.33	2.32
AlVI	0.25	0.32	0.34	0.34	0.18	0.24	0.32	0.36	0.00	0.00	0.03	0.03	0.04	0.00	0.02	0.06
Ti	0.41	0.43	0.36	0.38	0.45	0.40	0.39	0.38	0.46	0.44	0.45	0.43	0.46	0.44	0.44	0.46
Fe^{3+}	0.34	0.42	0.35	0.41	0.37	0.37	0.40	0.42	0.36	0.32	0.33	0.34	0.36	0.32	0.36	0.38
Mn	0.12	0.12	0.12	0.13	0.12	0.11	0.11	0.12	0.11	0.09	0.11	0.08	0.12	0.12	0.11	0.11
Mg	0.47	0.50	0.47	0.54	0.51	0.51	0.51	0.49	0.96	0.97	0.94	0.93	0.96	0.94	0.96	0.93
Fe^{2+}	4.17	3.90	4.05	3.91	4.15	4.07	3.96	3.90	3.83	3.98	3.85	3.94	3.79	3.99	3.84	3.74
Na	0.05	0.02	0.02	0.03	0.04	0.04	0.03	0.03	0.02	0.01	0.02	0.02	0.02	0.04	0.03	0.02
K	2.03	2.00	2.02	1.96	1.99	2.01	1.99	1.97	1.93	1.92	2.04	1.99	1.96	1.95	1.96	1.98
Ca	0.00	0.00	0.00	0.01	0.00	0.01	0.00	0.01	0.04	0.00	0.00	0.00	0.01	0.01	0.01	0.01
F	0.60	0.54	0.35	0.49	0.57	0.44	0.53	0.48	0.26	0.17	0.40	0.32	0.39	0.41	0.38	0.42
Cl	0.05	0.04	0.03	0.04	0.04	0.04	0.04	0.05	0.02	0.03	0.02	0.03	0.03	0.02	0.03	0.02
OH	3.35	3.41	3.62	3.47	3.39	3.52	3.43	3.47	3.72	3.80	3.58	3.65	3.59	3.57	3.59	3.56
H_2O%	3.03	3.12	3.31	3.18	3.09	3.13	3.15	3.20	3.37	3.48	3.28	3.34	3.29	3.26	3.30	3.29
Fe/(Fe + Mg)	0.91	0.90	0.90	0.89	0.90	0.90	0.90	0.90	0.81	0.82	0.82	0.82	0.81	0.82	0.81	0.82
T °C	623	633	613	621	631	623	623	622	645	635	642	633	645	635	639	647
P (GPa)	0.2	0.3	0.3	0.3	0.2	0.2	0.2	0.3	0.1	0.2	0.1	0.1	0.2	0.1	0.1	0.1
H_2Ocalc	3.03	3.12	3.31	3.18	3.09	3.13	3.15	3.20	3.37	3.48	3.28	3.34	3.29	3.26	3.30	3.29
fO_2	−11.42	−9.40	–	–	–	–	–	–	−10.10	−11.42	−9.40	−12.00	−10.50	−10.50	−12.74	−11.42
AIS	1.26	1.35	1.37	1.36	1.26	1.28	1.33	1.35	1.18	1.24	1.16	1.19	1.21	1.16	1.16	1.17
Mg# (OC)	9	10	10	11	10	10	10	10	19	18	18	18	19	18	19	18

Table 3
U–Th abundance and U–Pb zircon ages for Lombel and Badesi biotite granite.

	(ppm)	(ppm)	Ratio	Ratio	±1σ (%)	Ratio	±1σ (%)	Ratio	±1σ (%)	Age (Ma)	±1σ (%)	Age (Ma)	±1σ (%)	Age (Ma)	±1σ (%)
	Th	U	Th/U	$^{207}Pb/^{206}Pb$	$^{207}Pb/^{206}Pb$	$^{207}Pb/^{235}U$	$^{207}Pb/^{235}U$	$^{206}Pb/^{238}U$	$^{206}Pb/^{238}U$	$^{207}Pb/^{206}Pb$	$^{207}Pb/^{206}Pb$	$^{207}Pb/^{235}U$	$^{207}Pb/^{235}U$	$^{206}Pb/^{238}U$	$^{206}Pb/^{238}U$
Lombel biotite granite															
LBL1-01	154	309	0.5	0.0579	0.0014	0.6632	0.0160	0.0832	0.0007	528	58.3	517	9.8	515	4.0
LBL1-02	107	177	0.6	0.0590	0.0020	0.7342	0.0251	0.0905	0.0010	565	67.6	559	14.7	559	5.9
LBL1-03	10,180	8513	1.2	0.0947	0.0017	0.5914	0.0079	0.0458	0.0006	1524	39.4	472	5.1	289	4.0
LBL1-04	3337	4459	0.8	0.1342	0.0026	0.5282	0.0117	0.0287	0.0005	2153	33.3	431	7.8	183	3.3
LBL1-05	169	440	0.4	0.1651	0.0047	1.4615	0.0405	0.0643	0.0006	2508	47.1	915	16.7	402	3.5
LBL1-06	33	45.2	0.7	0.0595	0.0039	0.7841	0.0466	0.0907	0.0016	587	144.0	588	26.5	560	9.4
LBL1-07	275	410	0.7	0.0618	0.0022	0.7778	0.0248	0.0906	0.0010	733	75.9	584	14.2	559	6.1
LBL1-08	464	1064	0.4	0.0642	0.0013	0.6788	0.0145	0.0767	0.0008	746	42.6	526	8.8	476	5.0
LBL1-09	100	167	0.6	0.0613	0.0028	0.6082	0.0285	0.0726	0.0015	650	97.1	482	18.0	452	9.3
LBL1-10	66	106	0.6	0.0584	0.0025	0.7302	0.0314	0.0916	0.0012	543	90.6	557	18.4	565	6.9
LBL1-11	116	130	0.9	0.0629	0.0026	0.7933	0.0322	0.0918	0.0011	706	85.9	593	18.3	566	6.7
LBL1-12	851	1851	0.5	0.0733	0.0017	0.9295	0.0172	0.0926	0.0012	1033	78.7	667	9.0	571	7.1
LBL1-13	105	154	0.7	0.0580	0.0020	0.7271	0.0245	0.0914	0.0010	528	78.7	555	14.4	564	5.7
LBL1-14	984	3243	0.3	0.0815	0.0014	1.0291	0.0207	0.0911	0.0007	1235	39.8	718	10.4	564	4.1
LBL1-15	37	72.5	0.5	0.0621	0.0033	0.7792	0.0359	0.0914	0.0014	680	113.0	585	20.5	564	8.0
LBL1-16	78	113	0.7	0.0600	0.0023	0.7762	0.0282	0.0945	0.0010	606	83.3	583	16.1	582	6.1
LBL1-17	69	100	0.7	0.0663	0.0028	0.8192	0.0313	0.0910	0.0011	817	88.9	608	17.5	561	6.5
LBL1-18	188	354	0.5	0.0698	0.0021	0.8177	0.0233	0.0855	0.0008	924	61.1	607	13.0	529	4.5
LBL1-19	207	253	0.8	0.0609	0.0020	0.6821	0.0216	0.0814	0.0008	635	70.4	528	13.0	505	4.6
LBL1-20	19	28.2	0.7	0.0564	0.0045	0.8271	0.0529	0.0979	0.0020	478	176.0	612	29.4	602	11.8
Badesi biotite granite															
BSI4-01	1828	3463	0.5	0.0722	0.0012	0.8884	0.0140	0.0893	0.0007	991	33.3	646	7.5	551	4.0
BSI4-02	819	1267	0.7	0.0654	0.0013	0.7499	0.0150	0.0833	0.0010	787	41.8	568	8.7	516	6.0
BSI4-03	94	126	0.7	0.0661	0.0026	0.8103	0.0307	0.0899	0.0011	809	88.0	603	17.2	555	6.6
BSI4-04	74	54.7	1.4	0.1805	0.0280	12.3157	3.1385	0.1776	0.0253	2658	260.0	2629	239.0	1054	139.0
BSI4-05	148	208	0.7	0.0595	0.0019	0.7330	0.0241	0.0895	0.0011	587	65.7	558	14.1	553	6.6
BSI4-06	318	494	0.6	0.0613	0.0014	0.8220	0.0190	0.0972	0.0009	650	50.0	609	10.6	598	5.3
BSI4-07	183	194	0.9	0.0716	0.0026	0.8972	0.0371	0.0897	0.0012	976	73.0	650	19.8	554	6.9
BSI4-08	896	1307	0.7	0.0652	0.0017	0.8089	0.0225	0.0894	0.0006	789	53.7	602	12.6	552	3.7
BSI4-09	164	246	0.7	0.0978	0.0060	1.2825	0.1061	0.0891	0.0015	1583	114.8	838	47.2	550	8.7
BSI4-10	85	129	0.7	0.0631	0.0038	0.7591	0.0380	0.0842	0.0012	722	129.6	573	22.0	521	7.4
BSI4-11	104	159	0.7	0.1608	0.0091	1.4470	0.0913	0.0629	0.0012	2465	96.0	909	37.9	393	7.4
BSI4-12	687	1037	0.7	0.0610	0.0012	0.8190	0.0162	0.0971	0.0007	639	42.6	607	9.1	597	4.3
BSI4-13	52	76.1	0.7	0.0715	0.0035	0.8596	0.0394	0.0892	0.0018	972	127.8	630	21.5	551	10.4
BSI4-14	1748	3207	0.5	0.0629	0.0013	0.7736	0.0165	0.0891	0.0009	703	44.4	582	9.5	550	5.5
BSI4-15	666	1275	0.5	0.0656	0.0014	0.7762	0.0156	0.0857	0.0007	794	43.4	583	8.9	530	4.4
BSI4-16	161	253	0.6	0.0595	0.0018	0.7381	0.0236	0.0897	0.0010	587	66.7	561	13.8	554	5.9
BSI4-17	55	81	0.7	0.0585	0.0036	0.7624	0.0395	0.0905	0.0014	550	135.0	575	22.7	558	8.6
BSI4-18	209	336	0.6	0.0594	0.0018	0.7330	0.0213	0.0896	0.0010	583	69.4	558	12.5	553	5.8
BSI4-19	38	74.3	0.5	0.0671	0.0039	0.8089	0.0426	0.0899	0.0016	843	119.0	602	23.9	555	9.7
BSI4-20	112	105	1.1	0.0600	0.0031	0.7464	0.0405	0.0900	0.0012	611	111.1	566	23.5	555	6.9

Table 4
Zircon Lu–Hf isotopes for Lombel and Badesi biotite granite.

	$^{176}Yb/^{177}Hf$	±1σ	$^{176}Lu/^{177}Hf$	±1σ	$^{176}Hf/^{177}Hf$	±1σ	Age (Ma)	εHf(t)	±1σ	TDM1	TDM2	fLu/Hf
Lombel biotite granite												
LBL1-01	0.042585	0.000816	0.001439	0.000026	0.282579	0.000011	565	5.1	0.682442	963	1114	−1.0
LBL1-02	0.036751	0.000333	0.001295	0.000011	0.282568	0.000011	565	4.8	0.674731	975	1132	−1.0
LBL1-03	0.176166	0.001545	0.005910	0.000038	0.282617	0.000012	565	4.8	0.700111	1033	1132	−0.8
LBL1-04	0.144105	0.009363	0.004684	0.000277	0.282592	0.000011	565	4.3	0.740483	1035	1157	−0.9
LBL1-05	0.036189	0.000328	0.001230	0.000009	0.282584	0.000010	565	5.4	0.650104	951	1100	−1.0
LBL1-06	0.035020	0.000165	0.001203	0.000005	0.282619	0.000010	565	6.6	0.658385	901	1032	−1.0
LBL1-07	0.191162	0.003067	0.005258	0.000090	0.282711	0.000014	565	8.4	0.763442	863	934	−0.8
LBL1-08	0.083259	0.001268	0.002836	0.000038	0.282602	0.000011	565	5.4	0.683002	967	1098	−0.9
LBL1-09	0.043095	0.001098	0.001392	0.000026	0.282549	0.000010	565	4.0	0.666862	1006	1173	−1.0
LBL1-10	0.042658	0.000515	0.001439	0.000021	0.282585	0.000012	565	5.3	0.706694	954	1102	−1.0
LBL1-11	0.042809	0.000819	0.001365	0.000018	0.282571	0.000012	565	4.8	0.704710	973	1128	−1.0
LBL1-12	0.078811	0.000561	0.002720	0.000008	0.282547	0.000012	565	3.5	0.698550	1046	1205	−0.9
LBL1-13	0.027215	0.000121	0.000921	0.000001	0.282563	0.000012	565	4.7	0.686976	973	1135	−1.0
LBL1-14	0.133785	0.000687	0.004971	0.000040	0.282619	0.000010	565	5.2	0.658378	1002	1111	−0.9
LBL1-15	0.025721	0.000480	0.000848	0.000018	0.282598	0.000010	565	6.0	0.667269	922	1065	−1.0
LBL1-16	0.026916	0.000311	0.000875	0.000004	0.282558	0.000010	565	4.6	0.662357	979	1144	−1.0
LBL1-17	0.040909	0.000794	0.001306	0.000026	0.282593	0.000010	565	5.6	0.668436	940	1084	−1.0
LBL1-18	0.036476	0.000179	0.001165	0.000005	0.282547	0.000011	565	4.1	0.677246	1002	1172	−1.0
LBL1-19	0.056767	0.000955	0.001842	0.000036	0.282599	0.000013	565	5.7	0.720742	945	1083	−0.9
LBL1-20	0.024825	0.000162	0.000830	0.000001	0.282573	0.000011	565	5.1	0.680215	957	1114	−1.0
Badesi biotite granite												
BS14-01	0.100230	0.001151	0.003578	0.000043	0.282558	0.000010	552	3.3	0.665621	1054	1204	−0.9
BS14-02	0.120321	0.002709	0.003933	0.000069	0.282574	0.000012	552	3.7	0.708052	1040	1180	−0.9
BS14-03	0.028779	0.000213	0.000975	0.000006	0.282512	0.000010	552	2.6	0.661601	1045	1241	−1.0
BS14-04	0.054300	0.001858	0.001747	0.000048	0.282573	0.000014	552	4.5	0.761745	981	1138	−1.0
BS14-05	0.031331	0.000133	0.001029	0.000010	0.282542	0.000010	552	3.7	0.655471	1005	1183	−1.0
BS14-06	0.053656	0.001175	0.001648	0.000031	0.282555	0.000011	552	3.9	0.687959	1003	1170	−1.0
BS14-07	0.087777	0.001039	0.002765	0.000047	0.282553	0.000013	552	3.4	0.721887	1038	1198	−0.9
BS14-08	0.135495	0.004202	0.004172	0.000113	0.282594	0.000013	552	4.3	0.752964	1017	1146	−0.9
BS14-09	0.072756	0.000783	0.002255	0.000020	0.282534	0.000013	552	2.9	0.731067	1051	1225	−0.9
BS14-10	0.031628	0.000825	0.001045	0.000024	0.282560	0.000011	552	4.3	0.689243	981	1149	−1.0
BS14-11	0.073723	0.000625	0.002247	0.000011	0.282545	0.000015	552	3.3	0.776766	1035	1203	−0.9
BS14-12	0.075551	0.001343	0.002510	0.000029	0.282543	0.000011	552	3.2	0.688566	1044	1211	−0.9
BS14-13	0.028420	0.000598	0.000942	0.000013	0.282542	0.000012	552	3.7	0.691182	1002	1181	−1.0
BS14-14	0.070795	0.003576	0.002366	0.000100	0.282549	0.000010	552	3.4	0.667439	1032	1197	−0.9
BS14-15	0.053898	0.000766	0.001714	0.000018	0.282530	0.000010	552	3.0	0.655663	1042	1222	−1.0
BS14-16	0.030287	0.000204	0.001050	0.000001	0.282558	0.000010	552	4.2	0.654759	983	1152	−1.0
BS14-17	0.025136	0.000290	0.000844	0.000004	0.282521	0.000011	552	3.0	0.670909	1029	1221	−1.0
BS14-18	0.031147	0.000338	0.001016	0.000006	0.282533	0.000010	552	3.3	0.652161	1018	1202	−1.0
BS14-19	0.022403	0.000351	0.000779	0.000015	0.282555	0.000009	552	4.2	0.647455	980	1153	−1.0
BS14-20	0.053413	0.001054	0.001741	0.000022	0.282538	0.000012	552	3.3	0.692776	1030	1205	−1.0

$Hfi=(^{176}Hf/^{177}Hf)_S((^{176}Lu/^{177}Hf)_S*(EXP(\lambda*t/1000)1)\varepsilon Hft=((^{176}Lu/^{177}Hf)_S((^{176}Hf/^{177}Hf)S*(EXP(\lambda*t/1000)1)))/((^{176}Hf/^{177}Hf)_{CHUR},0((^{176}Lu/^{177}Hf)_{CHUR},0*(EXP(\lambda*t/1000)-1)))*10,000.$

$T_{DM1} = (1/\lambda*LN(1+((^{176}Hf/^{177}Hf)_S-(^{176}Hf/^{177}Hf)_{DM})/((^{176}Lu/^{177}Hf)S-(^{176}Lu/^{177}Hf)_{DM})).$

$T_{DM2} = T_{DM1}(T_{DM1}\text{-}t/1000)*((f_{CC}-((^{176}Lu/^{177}Hf)S/((^{176}Lu/^{177}Hf)_{CHUR}\text{-}1))/(f_{CC} \times f_{DM}).$

TDM2 have been adopted as stage model.

$(^{176}Hf/^{177}Hf)_S$, $(^{176}Lu/^{177}Hf)_S$ measured values; $(^{176}Lu/^{177}Hf)_{CHUR} = 0.0336 \pm 1$, $(^{176}Hf/^{177}Hf)_{CHUR} = 0.282785 \pm 11$ (Bouvier et al., 2008).

$(^{176}Lu/^{177}Hf)_{DM} = 0.0384$, $(^{176}Hf/^{177}Hf)_{DM} = 0.28325$ (Griffin et al., 2000).

$f_{CC} = -0.548$ (composition of continental crust), $f_{DM} = 0.16$; $\lambda = 1.867 \times 10^{-11}$ $year^{-1}$ calculations based on (Soderlund et al., 2004), t = intrusion age.

experimental details and supplimentary file of this article.

4.3. Zircon Lu–Hf isotopic analysis

Zircon crystals from the biotite granites of the Lombel and Badesi massifs were analyzed for *in situ* Hf isotope ratios. This analysis was performed with the aid of a NeptunePlus MC–ICP–MS (Thermo Fisher Scientific, Germany) together with a Geolas HD excimer ArF laser ablation device (Coherent, Gottingen, Germany) at Wuhan Sample Solution Analytical Technology Co., Ltd., Hubei, China. Included in the laser ablation system is a wire signal smoothing device that produces smooth signals at a very low repetition rate, down to 1 Hz (Hu et al., 2015). Helium was applied as the carrier gas in the ablation cell together with argon (makeup gas). The sensitivity of Hf isotopes was improved by the addition of a small amount of nitrogen to the argon makeup gas (Hu et al., 2015). Based on the standard arrangement, the introduction of nitrogen together with the use of the recently designed X skimmer cone and Jet sample cone in Neptune Plus ameliorated the signal intensity of Hf, Yb, and Lu by factors of 5.3, 4.0, and 2.4, respectively. The results were obtained for zircon in a single spot ablation mode at a spot size of 44 μm, close to those for U–Pb dating. Detail in the supplementary file of this article.

4.4. Whole–rock major- and trace–element analyses

Samples from the Lombel and Badesi massifs were crushed and powdered to b200 mesh in an agate mill. To obtain the major elements, X–Ray Fluorescence (XRF) (Primus II, Rigaku, Japan) was performed at the Wuhan Sample Solution Analytical Technology Co., Wuhan, China. Chinese national standards were used to ascertain the precision and accuracy of the XRF data, with an analytical uncertainty of $< 5\%$ and a detection limit of $< 0.01\%$. Duplicate runs on selected samples were estimated at $\sim 1\%$ for N10 wt% and 5% for the concentrations of other major elements. The details of the XRF method are described in Ma et al. (2012).

Whole–rock trace and rare earth–element (REE) analyses were performed using an Agilent 7700e ICP–MS at Wuhan Sample Solution Analytical Technology Co., Ltd., Wuhan, China, following the

Table 5
Major (wt %) and trace elements compositions (ppm) for Lombel and Badesi biotite granite. Note, TFe_2O_3 = FeOt/0.8998, XFeO* = FeO*/(FeO* + MgO).

Samples#	biotite granite Lombel massif					Biotite granite Badesi massif		
	LBL-1	GLBL-7	LBL-13	LBL-20	LBL-21	BSI-4	BSI-10	BSI-14
SiO_2	75.65	74.97	78.04	76.67	73.67	75.77	73.47	76.08
TiO_2	0.10	0.15	0.10	0.07	0.22	0.12	0.07	0.02
Al_2O_3	12.86	12.77	11.74	12.52	12.93	12.68	14.20	12.98
TFe_2O_3	1.69	2.11	1.50	1.76	2.43	1.75	1.34	0.98
MgO	0.06	0.12	0.05	0.05	0.21	0.11	0.04	0.01
MnO	0.03	0.04	0.03	0.03	0.04	0.03	0.02	0.01
CaO	0.52	0.64	0.28	0.47	0.65	0.65	0.65	0.43
Na_2O	3.63	3.59	3.12	3.91	3.51	3.52	4.04	4.52
K_2O	5.04	5.00	4.27	4.57	5.13	5.00	5.79	4.08
P_2O_5	0.01	0.03	0.02	0.01	0.05	0.02	0.01	0.01
SO_3	0.01	0.01	0.01	0.01	0.01	0.01	0.01	0.01
LOI	0.39	0.29	0.74	0.45	0.52	0.03	0.24	0.03
Total	99.60	99.40	99.20	100.10	98.80	99.70	99.60	99.10
Mg#	7.64	11.70	7.21	6.21	16.80	12.80	5.50	2.32
FeOT	1.52	1.90	1.35	1.58	2.19	1.57	1.21	0.88
Fe_2O_3T	1.69	2.11	1.50	1.35	1.86	1.34	1.02	0.75
FeO	1.29	1.61	1.15	1.35	1.86	1.34	1.02	0.75
Fe_2O_3	0.23	0.28	0.20	0.24	0.33	0.24	0.18	0.13
$Na_2O + K_2O$	8.67	8.59	7.39	8.48	8.64	8.52	9.83	9.60
K_2O/Na_2O	1.38	1.39	1.36	1.16	1.46	1.42	1.43	0.90
XFeO*	1.0	0.9	1.0	1.0	0.9	0.9	1.0	1.0
Li	26.70	33.80	32.00	16.70	13.10	18.70	11.50	2.69
Be	6.13	6.26	5.36	6.20	4.73	4.62	6.60	8.63
Sc	1.09	2.02	1.59	0.56	2.60	1.12	0.48	0.81
V	2.69	4.76	8.02	2.02	7.26	5.34	1.81	1.94
Cr	15.70	13.30	13.10	16.20	13.20	25.10	14.00	21.10
Co	0.60	0.93	0.85	0.46	1.35	0.83	0.44	0.20
Ni	1.94	1.83	9.07	1.48	2.06	2.07	2.61	1.40
Cu	208.00	17.10	65.30	12.20	36.00	2.46	8.41	1.75
Zn	37.80	45.20	30.00	48.40	54.80	29.90	22.70	16.20
Ga	23.10	22.90	19.40	24.20	22.50	20.70	24.70	24.70
Rb	215.00	202.00	231.00	260.00	161.00	161.00	231.00	328.00
Sr	28.90	48.90	35.20	9.53	73.90	56.60	28.20	8.50
Y	64.70	66.10	53.10	95.50	59.60	38.60	69.50	103.00
Zr	206.00	214.00	129.00	267.00	316.00	178.00	124.00	313.00
Nb	36.70	34.10	33.00	109.00	35.80	23.90	44.60	93.00
Sn	4.31	4.39	5.50	6.56	4.24	2.13	3.85	4.47
Cs	1.73	1.85	1.87	1.21	1.05	1.18	1.87	1.49
Ba	161.00	311.00	187.00	43.20	437.00	335.00	131.00	52.90
La	57.20	63.90	22.60	26.70	58.00	47.60	47.30	14.10
Ce	113.00	130.00	52.60	61.40	116.00	94.40	87.80	36.50
Pr	13.20	14.90	5.99	6.88	13.40	10.40	12.10	4.44
Nd	44.60	51.20	21.90	24.70	48.00	36.10	42.70	16.10
Sm	9.10	10.50	5.04	7.00	10.30	6.62	9.46	4.20
Eu	0.44	0.73	0.43	0.18	0.98	0.69	0.46	0.06
Gd	8.08	9.49	4.74	8.18	9.35	5.82	8.45	5.14
Tb	1.47	1.62	0.96	2.00	1.63	1.00	1.60	1.21
Dy	9.68	10.60	6.73	14.80	10.10	6.18	10.10	9.34
Ho	2.03	2.18	1.53	3.47	2.08	1.30	2.21	2.37
Er	6.38	6.67	5.24	11.40	6.04	4.09	7.39	10.20
Tm	1.00	0.99	0.96	1.89	0.92	0.63	1.19	2.34
Yb	7.00	7.13	7.77	13.50	6.32	4.22	8.74	21.00
Lu	1.08	1.07	1.30	2.03	0.91	0.63	1.28	4.13
Hf	6.80	6.87	5.17	11.30	9.02	5.42	5.26	19.20
Ta	2.11	2.27	2.90	4.22	2.05	1.57	2.65	3.31
Tl	1.07	1.00	1.21	1.27	0.80	0.84	1.10	0.59
Pb	112.00	89.80	74.20	89.70	45.00	31.10	39.80	62.90
Th	20.10	22.70	26.40	61.70	17.30	14.80	48.80	62.70
U	3.69	3.76	7.16	10.00	2.50	2.33	7.18	35.30
$\sum$REE	339.00	377.00	190.00	279.00	343.00	258.00	310.00	233.00
$(La/Sm)_N$	4.10	3.94	2.89	2.46	3.63	4.64	3.22	2.16
$(La/Yb)_N$	5.86	6.43	2.10	1.42	6.58	8.10	3.88	0.48
$(Gd/Lu)_N$	0.92	1.09	0.44	0.49	1.27	1.14	0.81	0.15
Eu*	0.05	0.07	0.09	0.02	0.10	0.11	0.05	0.01
Ga/Al	3.39	3.38	3.12	3.65	3.28	3.08	3.28	3.60
Y/Nb	1.76	1.93	1.60	0.87	1.66	1.61	1.55	1.10
Sr/Y	0.45	0.74	0.66	0.10	1.24	1.47	0.41	0.08
Nb/U	9.95	9.07	4.61	10.90	14.32	10.26	6.21	2.63
K	1.13	1.10	0.49	0.38	1.70	1.78	0.67	0.10
Ce/Nb	3.07	3.81	1.59	0.56	3.24	3.94	1.96	0.39

Table 6
Sm–Nd and Rb–Sr isotopic compositions for Lombel and Badesi biotite granite.

	Rb (ppm)	Sr (ppm)	Rb/Sr	$^{87}Rb/^{86}Sr$	$^{87}Sr/^{86}Sr$	t (Ma)	Isr	εSr(t)	Sm (ppm)	Nd (ppm)	Sm/Nd	$^{147}Sm/^{144}Nd$	$^{143}Sm/^{144}Nd$	INd	εNd (t)	TDM (Ga)	T2DM (Ga)	fSm/Nd
Sample#																		
LBL 1	215	28.9	7.4	21.309402	0.874707	560	0.70458	10.37964	9.1	44.6	0.2	0.123316	0.512449	0.511997	1.6	1.2	1.2	−0.4
LBL 21	161	73.9	2.2	6.288894	0.753482	560	0.70327	−8.17187	10.3	48.0	0.2	0.129731	0.512457	0.511981	1.3	1.3	1.2	−0.3
BSI 4	161	56.6	2.8	8.280071	0.769583	560	0.70348	−5.27309	6.6	36.1	0.2	0.111011	0.512413	0.512006	1.8	1.1	1.1	−0.4
BSI 10	231	28.2	8.2	24.134806	0.894810	560	0.70212	−24.48830	9.5	42.7	0.2	0.133881	0.512515	0.512024	2.1	1.2	1.1	−0.3

procedures described by Liu et al. (2008). Pure Rb standard solution was considered for internal calibration, whereas GSR-1, BHVO2, and OU-6 for the reference materials. For most elements, the estimated relative errors of ICP–MS were better than ± 5–10%.

4.5. Sr–Nd isotope analyses

Whole–rock Sr–Nd isotope analyses were carried out on biotite granites from the Lombel and Badesi massifs. These analyses were conducted using a Neptune Plus MC–ICP–MS (Thermo Fisher Scientific, Bremen, Germany) equipped with a Geolas HD excimer ArF laser ablation system (Coherent, Göttingen, Germany) at Wuhan Sample Solution Analytical Technology Co., Ltd., Hubei, China. Detailed analytical procedures have been described by Xu et al. (2015). Detail information in the supplementary file.

4.6. Temperatures, pressures, depths, and fO_2 calculations

The major–element compositions of biotite were first computerized on the Excel worksheet of Zhang 2003; Table 4) to obtain the atoms per formula unit (apfu). These apfu values permitted biotite temperatures, pressures, and H_2O contents to be estimated using Eqns. 1 and 2 of Luhr et al. (1984) and Uchida et al. (2007), respectively. The whole-rock temperatures, pressures, and depths for the Lombel and Badesi massifs were calculated using the excel worksheet of Yang et al. (2021; Table 5).

$$T(K) = \frac{838}{1.0337 - \frac{Ti}{Fe^{2+}}} \quad (1)$$

$$P(kbar) = 3.33Al^{T} - 6.53(\pm 0.33) \quad (2)$$

P: pressure in kilobar, *T:* temperature in Kelvin, Al^{T}*:* total Al in biotite, *Ti* and Fe^{2+} are Ti and Fe^{2+} in biotite.

5. Results

5.1. Biotite chemical composition

The analyzed biotite crystals are ferroan and yield relatively high Fe/(Fe+Mg) ratios > 0.80 (Table 2). Based on the classification diagram defined by four end-members, including phlogopite, K_2Mg_6 $[Al_2Si_6O_{20}](OH)_4$; annite, $K_2Fe^{2+6}[Al_2Si_6O_{20}](OH)$; eastonite, $K_2Mg[Al](OH)$; and siderophillite, $K_2Fe^{2+4}Al_2[Al_4Si_4O_{20}](OH)_4$ (Rieder et al., 1999), biotite crystals from both massifs plot near the annite field (Fig. 6a). The biotite crystals of the Lombel Granite are depleted in MgO (1.9–2.2 wt%) relative to Al_2O_3 (13.3–14.6 wt%). Its total FeO and FeO/MgO ratio range from 31.4 to 32.8 wt% and 14.3–17.1, respectively. Comparatively, biotites of the Badesi Granite registered high MgO (3.8–3.9 wt%) and low Al_2O_3 (12.1–12.6 wt%) contents. Biotite from the Badesi Granite has total FeO and FeO/MgO ratios of 30.3–31.5 wt% and 7.7–8.2, respectively, which are slightly lower than those of the Lombel massif. Crystals from both granites are CaO-, Na_2O-, and MnO-depleted, but enriched in K_2O, TiO_2, and SiO_2 (Table 2). The estimated Mg# from both the Lombel and Badesi massifs resemble (0.09–0.19; Table 2) and plot in the alkaline field (Fig. 6b). Fig. 6c and d shows that the samples plotted in the anorogenic alkaline field, confirming their post-tectonic characteristics in the Babouri–Figuil magmatic complex.

The F and Cl abundances in Lombel granite ranging from 0.4 to 0.6 apfu and 0.04–0.1 apfu, respectively, are relatively higher than those in biotite from the Badesi Granite ranging from 0.2 to 0.4 apfu and 0.02–0.03 apfu, respectively. The studied biotites can be classified as Cl–depleted varieties, different from Cl–rich biotites. The analyzed biotite crystals were unaltered and host zircon crystals (Fig. 6e and f).

5.2. Zircon morphology and U–Pb age

CL images of 40 zircon crystals from the Lombel Granite (LBL-1) and

Table 7
Calculated ratios and P–T values for Lombel and Badesi biotite granite. A/CNK = molar (Al_2O_3)/(CaO + Na_2O + K_2O) ratio; A/NK = molar (Al_2O_3)/(Na_2O + K_2O) ratio; σ = (Na_2O + K_2O)^2/(SiO_2- 43), unit in wt%; ∑diXi, where di is oxide i coefficient, and Xi is its mole fraction.

Biotite granite								
Ratios	LBL1	GLBL7	LBL 13	LBL 20	LBL-21	BSI-4	BSI-10	BSI-14
A/CNK 1	1.0	1.0	1.1	1.0	1.0	1.0	1.0	1.0
A/NK 2	1.1	1.1	1.2	1.1	1.1	1.1	1.1	1.1
σ3	2.3	2.3	1.6	2.1	2.4	2.2	3.2	2.2
∑diXi	−1.7	−1.7	−1.7	−1.7	−1.7	−1.7	−1.7	−1.7
T (°K)	1122	1122	1082	1155	1172	1100	1054	1177
T (°C)	848	848	809	882	899	827	781	904
ΔQFM (high T)	−0.6	−0.6	−0.6	−0.6	−0.6	−0.6	−0.6	−0.6
logfO_2	−14.0	−14.0	−14.8	−13.3	−13.0	−14.4	−15.4	−12.9
log (Fe_2O_3/FeO)	−0.7	−0.7	−0.7	−0.7	−0.7	−0.7	−0.8	−0.7
Fe_2O_3/FeO (molar ratio)	0.2	0.2	0.2	0.2	0.2	0.2	0.2	0.2
Fe_2O_3/FeO (wt% ratio)	0.4	0.4	0.4	0.4	0.4	0.4	0.4	0.4
Fe_2O_3/(FeO + Fe_2O_3) (wt% ratio)	0.3	0.3	0.3	0.3	0.3	0.3	0.3	0.3
Fe^{3+}#	0.2	0.2	0.2	0.2	0.2	0.2	0.2	0.2
PQtz	156	164	228	133	195	136	525	181
P (Ab + Or)	148	156	236	125	186	128	515	172
P (MPa) (average)	152	160	232	129	190	132	520	177
P (kb)	1.5	1.6	2.3	1.3	1.9	1.3	5.2	1.8
P (GPa)	0.15	0.16	0.23	0.13	0.19	0.13	0.52	0.18
Emplacement depth (km)	4.1	4.3	6.3	3.5	5.1	3.6	14.0	4.8

Badesi Granite (BSI-4) show euhedral–prismatic pyramidal and/or bipyramidal internal structures. Their sizes ranged from ~ 100 to 250 μm. Most crystals showed oscillatory zoning with color differences in the cores and rims (Fig. 7a and b). Their U and Th contents varied significantly (Table 3).

The U and Th contents in zircons from Lombel Granite resemble and range from 28.2 to 8513 ppm and 19.1–10180 ppm, respectively. The Th/U ratios in these samples vary from 0.3 to 1.2 with most of the magnitudes being less than 0.7. Twenty zircon spots were analyzed and yielded $^{206}Pb/^{238}U$ zircon ages from 183 ± 2.2 to 602 ± 11.8 Ma. The high $^{206}Pb/^{238}U$ variations could be due to Pb mobilization by hydrous fluids. Eight crystals yielded a calculated U-Pb Concordia age of 566 ± 2.5 Ma and a corresponding mean square of weighted deviation MSWD = 1.6; this provided the emplacement age for this rock (Fig. 7c).

In the Badesi biotite granite, the U and Th contents were similar and ranged from 54 to 3463 ppm and 37–1828 ppm, respectively. The Th/U ratios vary from 0.5 to 1.3 with most values being less than 0.68. Twenty zircon crystals were analyzed and yielded $^{206}Pb/^{238}U$ ages from 393 ± 7.4 to 1054 ± 139 Ma. The high $^{206}Pb/^{238}U$ variation is presumably as previously stated. Seven zircon crystals yielded ages from 550 ± 5.5 to 558 ± 8.6 Ma, with a U-Pb Concordia age of 555 ± 2.7 Ma, corresponding to a mean square of weighted deviation MSWD = 2.1 and interpreted as the emplacement age of this rock (Fig. 7d).

5.3. Zircon Lu–Hf isotopes

Table 4 presents the *in situ* Hf isotopic compositions of individual zircon crystals dated from the Lombel and Badesi biotite granites. The $^{176}Hf/^{177}Hf$ ratios for the Lombel biotite granite varied from 0.282547 to 0.282711. Except for four crystals, they dominantly show relatively low $^{176}Yb/^{177}Hf$ ratios (< 0.1) and yield initial Hf values [$\varepsilon_{Hf}(t)$ = +3.5 to +8.4] with a weighted mean value of +5.2. The corresponding single-stage model (TDM1) age is ~ 1 Ga, and the two-stage modal (TDM2) age is ~ 1.2 Ga.

The $^{176}Hf/^{177}Hf$ ratios for 20 zircon crystals from the Badesi biotite granite range from 0.282512 to 0.282595, whereas $^{76}Yb/^{177}Hf$ ratios are < 0.08 (Table 4). Besides the three analyzed crystals, most of the zircons yielded initial Hf values [$\varepsilon_{Hf}(t)$ = +2.6 to +4.5] with a weighted mean value of +3.6. The corresponding TDM1 and TDM2 ages are ~ 1.0 Ga and 1.2 Ga, respectively.

5.4. Major & trace–elements

The studied granites have relatively high SiO_2 content of 73.7–78.0 wt% for the Lombel massif and 73.5–76.1 wt% for the Badesi massif. Al_2O_3 content varies from 11.7 to 12.9 wt% and 12.7–14.2 wt%, respectively, in those two massifs (Table 5). Both massifs show moderate total Fe_2O_3 contents of 1.5–2.4 and 0.9–1.8 wt%, respectively. The Na_2O (3.5–4.5 wt%) and K_2O (4.1–5.8 wt%) contents of samples from the Badesi massif are higher than those of most samples from the Lombel massif (Table 5). In these massifs, K_2O > Na_2O, the K_2O/Na_2O ratios vary from to 0.9–1.5, and the total alkali Na_2O + K_2O wt% from 7.4 to 9.8, with an average of 8.6 wt%. All the studied samples plot in the granite field in Na_2O + K_2O *vs.* SiO_2 and in the high–K series field, except for a single sample that registered an exceptionally high K_2O value, which plots in the shoshonite series field in K_2O *vs.* SiO_2 (Fig. 8a and b).

The studied granite samples from the two massifs are slightly peraluminous with an A/CNK ratio of modal Al_2O_3/(CaO+Na_2O+K_2O) > 1 and plot close to the line that divides the field of both peraluminous and metaluminous lithologies in the A/(CNK) *vs.* A/(NK) diagram (Fig. 8c). The samples have a Rittmann Serial Index [σ = (Na_2O + K_2O)^2 (SiO_2–43)] ranging from 1.6 to 3.2 (Table 5) and are placed within the sub- to mid-alkaline granite family, as per Fig. 8a. In the SiO_2 *vs.* Na_2O+K_2O–CaO diagram (Fig. 8d), most of the samples fell within the alkali-calcic field. Only two samples each fell into the alkali and calcic fields. The studied samples have low Mg# (< 18), high Fe-number [FeOt/(FeOt+MgO)] were registered for the Lombel massif (0.93–0.94) than the Badesi massif (0.88–0.89). Samples from both massifs plot in the Ferroan field (Fig. 8e). In the R1 *vs.* R2 classification diagram (Fig. 8f), the samples plotted in the alkali-granite field close to the line that divides this field from that of the granite. In the Harker binary diagrams (Fig. 9), Al_2O_3, Fe_2O_3, MgO, CaO, K_2O, and TiO_2 for the Lombel Granite samples correlated negatively with SiO_2, whereas Na_2O displayed a slight positive trend. However, a general negative trend was observed for rocks from both massifs, except for MnO and Na_2O.

The concentrations of high–field-strength elements (HFSE: Th, Nb, Ta, Ga, and Y) in all studied granites were relatively high (Table 5). Lower concentrations (< 10 ppm) were recorded for transition elements, e.g., Sc, V, Co, and Ni. Cr at 13.2–25.1 ppm, Rb at 161–328 ppm, Zr at 124–316 ppm, and Ba at 43.2–437 ppm is relatively higher. Intermediate to high values are those of Th (14.8–62.7 ppm), U (2.3–35.3 ppm), and Sr (8.50–73.9 ppm). The calculated ∑REE shows a moderate variation from 190 to 379 ppm. The La_N/Sm_N, La_N/Yb_N, and Gd_N/Lu_N ratios were 2.2–4.6, 0.5–8.1, and 0.2–1.3, respectively. In primitive mantle-

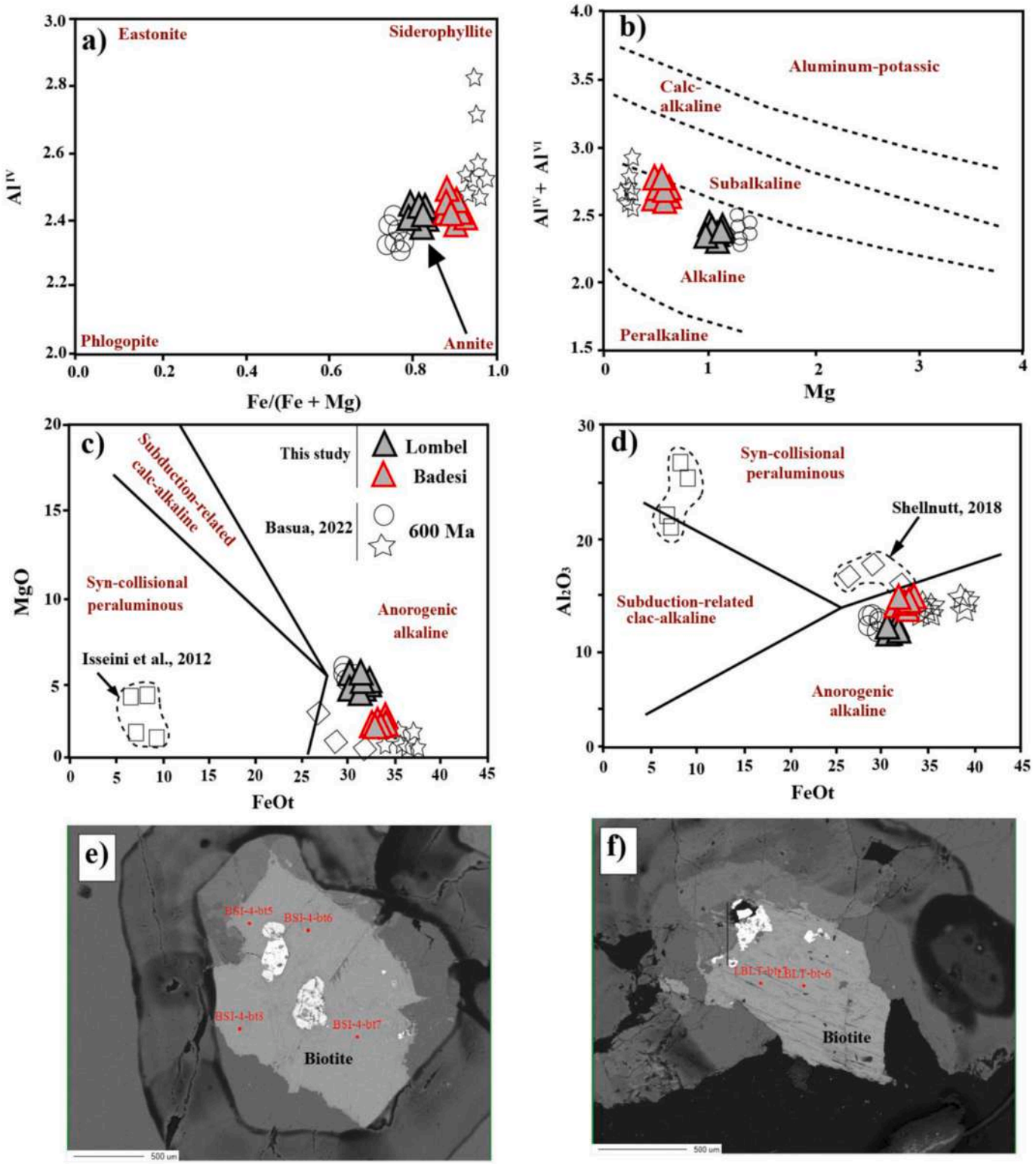

Fig. 6. Mineral chemistry plots of the studied granite from Lombel and Badesi massifs: (a) Fe/(Fe+Mg) versus Al^{IV} (Deer et al., 1992); (b) Mg versus Al^{IV} + Al^{VI} (Nachit et al., 1985); (c) FeOt versus MgO; (d) FeOt versus Al_2O_3; (e,f) BSE images of biotites from Lombel and Badesi massifs.

normalized spider diagram (Fig. 10a), Ba, P, Sr, Eu, and Ti are strongly depleted, whereas Nb, Ta, and other high field strength elements are depleted moderately. The negative anomalies for Ba, Sr, and Ti are possibly linked to the fractional crystallization of feldspar and iron oxides. The samples are relatively enriched in large ion lithophile elements (LILE) and light rare–earth elements (LREEs). These samples revealed positive anomalies in Rb, Th, U, and Pb (Fig. 10a). The chondrite–normalized REE plots in Fig. 10b show discerning patterns from light rare–earth elements (LREE) to middle rare–earth elements (MREE) and, conversely, ascending patterns from MREE–HREE. From Gd to Lu, the studied granites had enriched values relative to those of the upper and lower crustal averages. This confirms a weak REE fractionation for

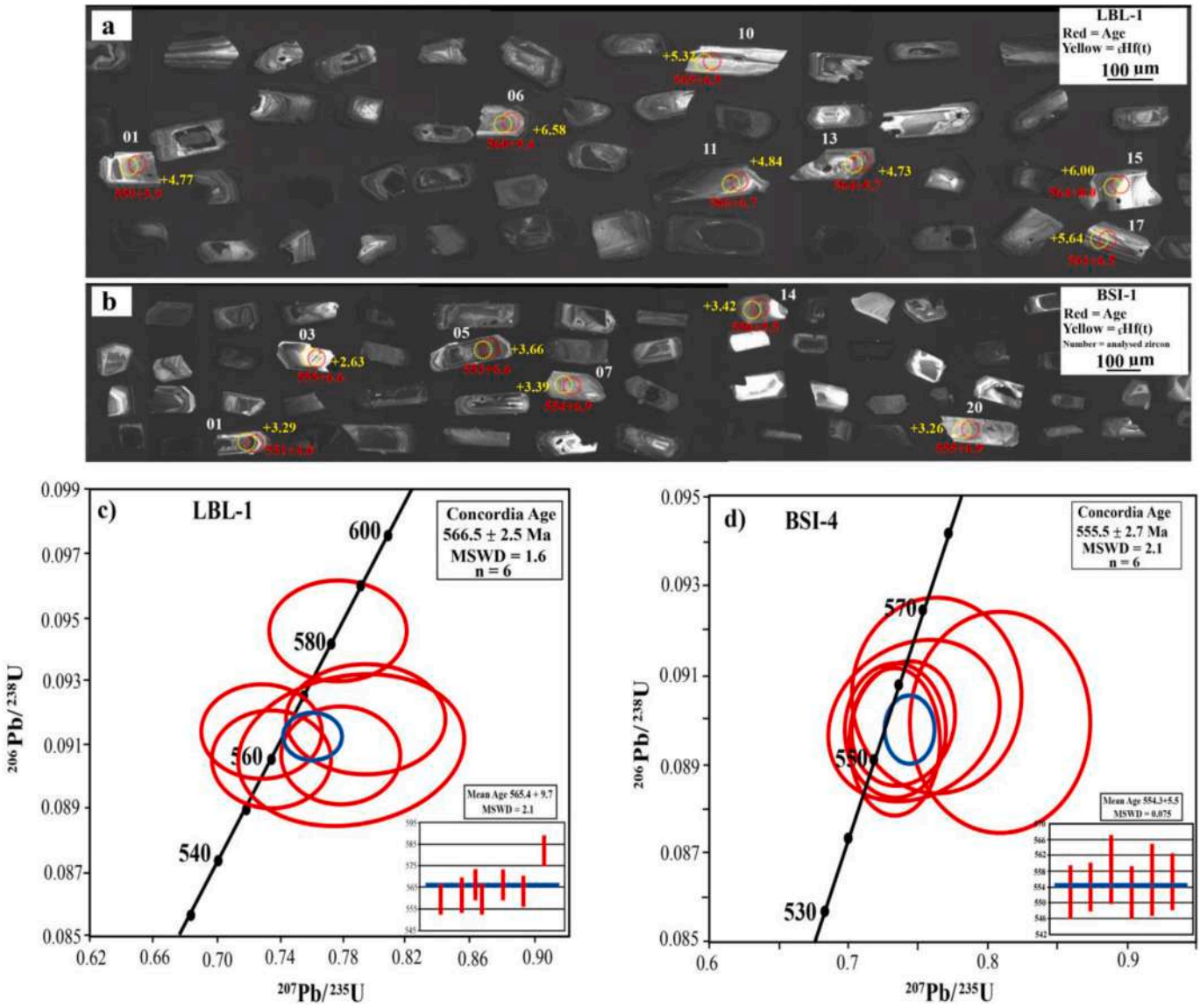

Fig. 7. (a,b) Cathodoluminescence (CL) images of selected zircons crystals of the studied A–type granite from the Lombel and Badesi massifs analyzed for U–Pb dating and Lu–Hf isotopes. Yellow dotted circles indicate analytical spots for the Lu–Hf isotopes and the red dotted circles represent analytical spots for the U–Pb dating. Zircon U–Pb Concordia plots of selected zircons crystals from the studied granite massifs analyzed for: (c) Lombel massif; (d) Badesi massif.

the studied granite, given that La_N/Yb_N varies from 0.5 to 8.1. Samples display deep negative Eu anomalies (Eu/Eu* = 0.01–0.1; Fig. 10b).

5.5. Sr–Nd isotopes

The Sr–Nd compositions were measured from the Lombel and Badesi massifs (two from each massif). The values obtained from both massifs are similar (Table 6). For the Lombel Granite, the $^{87}Sr/^{86}Sr$ (0.874707–0.753482) and $^{143}Nd/^{144}Nd$ (0.123316–0.129731) ratios were calculated, based on the obtained emplacement age at t = 560 Ma (Table 6). These yielded initial (Isr = 0.70458 and 0.70327) and initial ($\varepsilon_{Nd}(t)$ = +1.3 and + 1.6), respectively, with a corresponding Meso-proterozoic two–stage depleted mantle modal age (T2DM) of 1.2 Ga.

In contrast, samples from the Badesi massif recorded the following initial ratios for $^{87}Sr/^{86}Sr$ (0.769583–0.894810) and $^{143}Nd/^{144}Nd$ (0.70348–0.70212) that were calculated based on the obtained emplacement age at t = 560 Ma (Table 6). The recorded initial values Isr = 0.133881 and $\varepsilon_{Nd}(t)$ = +1.8 and + 2.1 resembles those obtained from the Lombel massif. They yielded a corresponding Mesoproterozoic two-stage mantle model age (T2DM) of 1.1 Ga (Table 6).

5.6. Temperatures, pressures, depths, and fO_2 calculations

The calculated biotite H_2O content ranged from 3.03 to 3.31 for the Lombel massif and from 3.26 to 3.48 for the Badesi massif (Table 7). Lower biotite temperatures from 613 to 633 °C were recorded for the Lombel massif than for the Badesi massif from 633 to 647 °C. Pressures for the Lombel massif from 200 to 280 MPa are high and wide relative to the low and constricted values from 120 to 160 MPa for the Badesi massif. Comparatively, whole–rock temperatures from 809 to 899 °C and 781–904 °C, pressures from 130 to 230 MPa and 130–520 MPa and depths of 3.5–6.3 and 3.6–14.0 km were highest for the Badesi massif relative to the Lombel massif, with the corresponding low fO_2 (ΔQFM -0.6) (Table 7).

6. Discussion

6.1. Tectonomagmatic setting of the Lombel and Badesi biotite granites

Granites from the Lombel and Badesi massifs were emplaced in an extensional setting. Therefore, they are parts of a regional emplacement

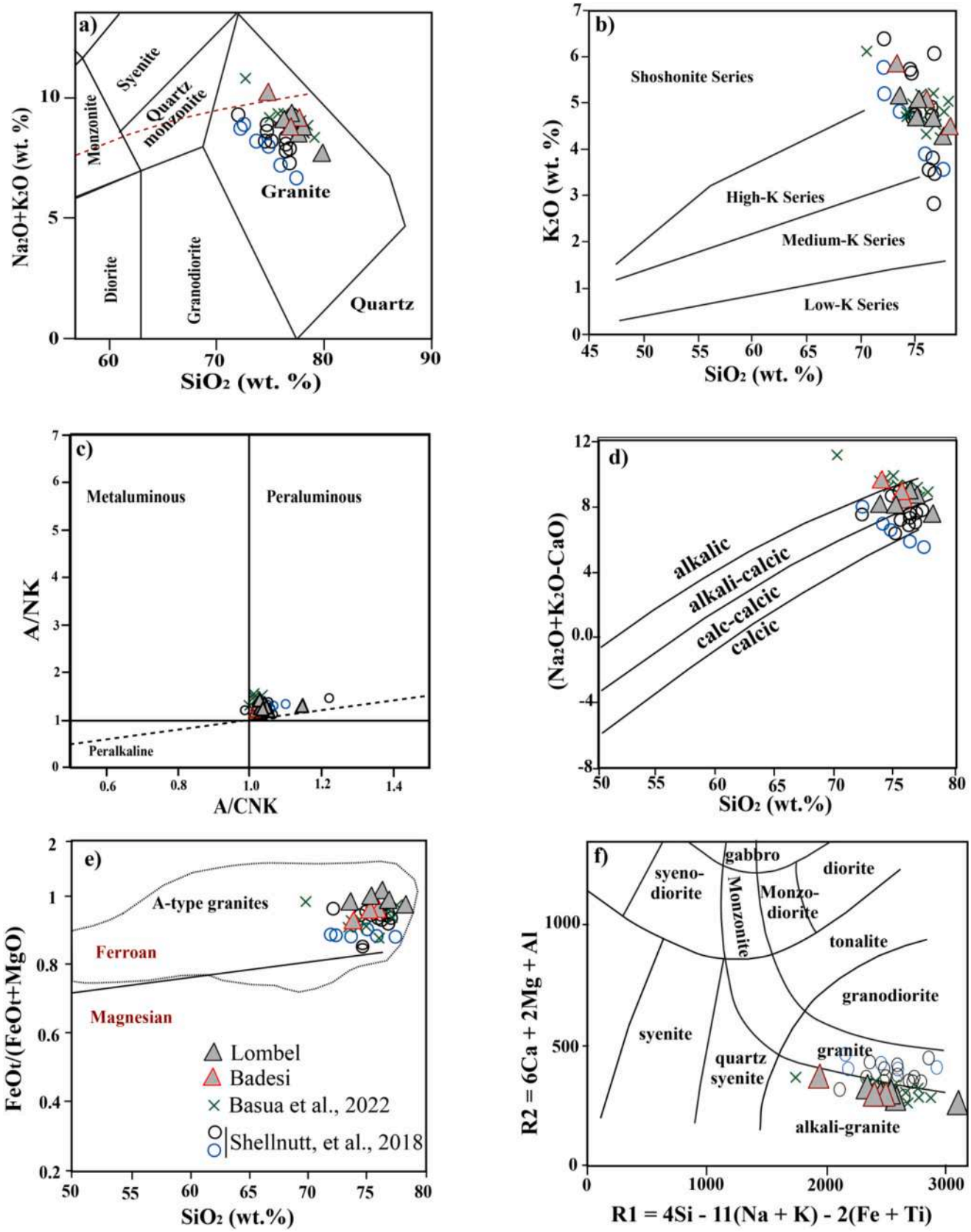

Fig. 8. Geochemical classification of the studied granite (triangles with black–bold lines: represent Lombel massif, triangles with red-bold lines: represent Badesi massif). (a) SiO_2 vs. $Na_2O + K_2O$ diagram of Le Maitre (1989), the red dash line as per Rittmann's (1973), (b) SiO_2 vs. K_2O diagram of Peccerillo and Taylor (1976), (c) A/CNK vs. A/NK diagram of Shand (1943); (d) SiO_2 vs. $Na_2O + K_2O$–CaO diagram (after Frost and Frost, 2001); (e) SiO_2 vs. FeOt/(FeOt + MgO) diagram (after Frost and Frost, 2001); (f) R1 vs. R2 diagram of De La Roche et al. (1980). Triangle plots = this study and circle plots = Shellnutt et al. (2018).

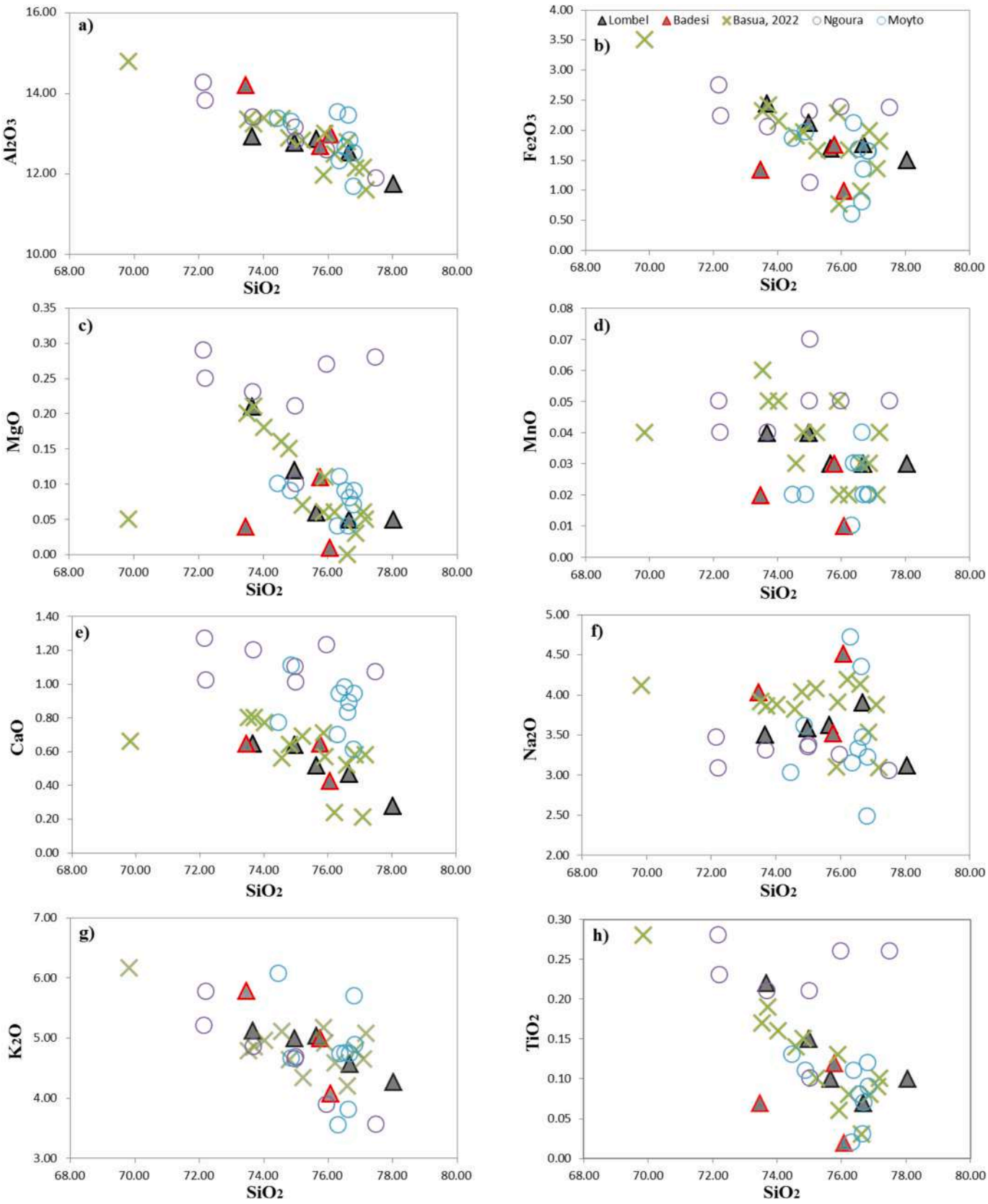

Fig. 9. Harker variation diagrams of major oxides (in wt%) of the studied granite versus SiO_2.

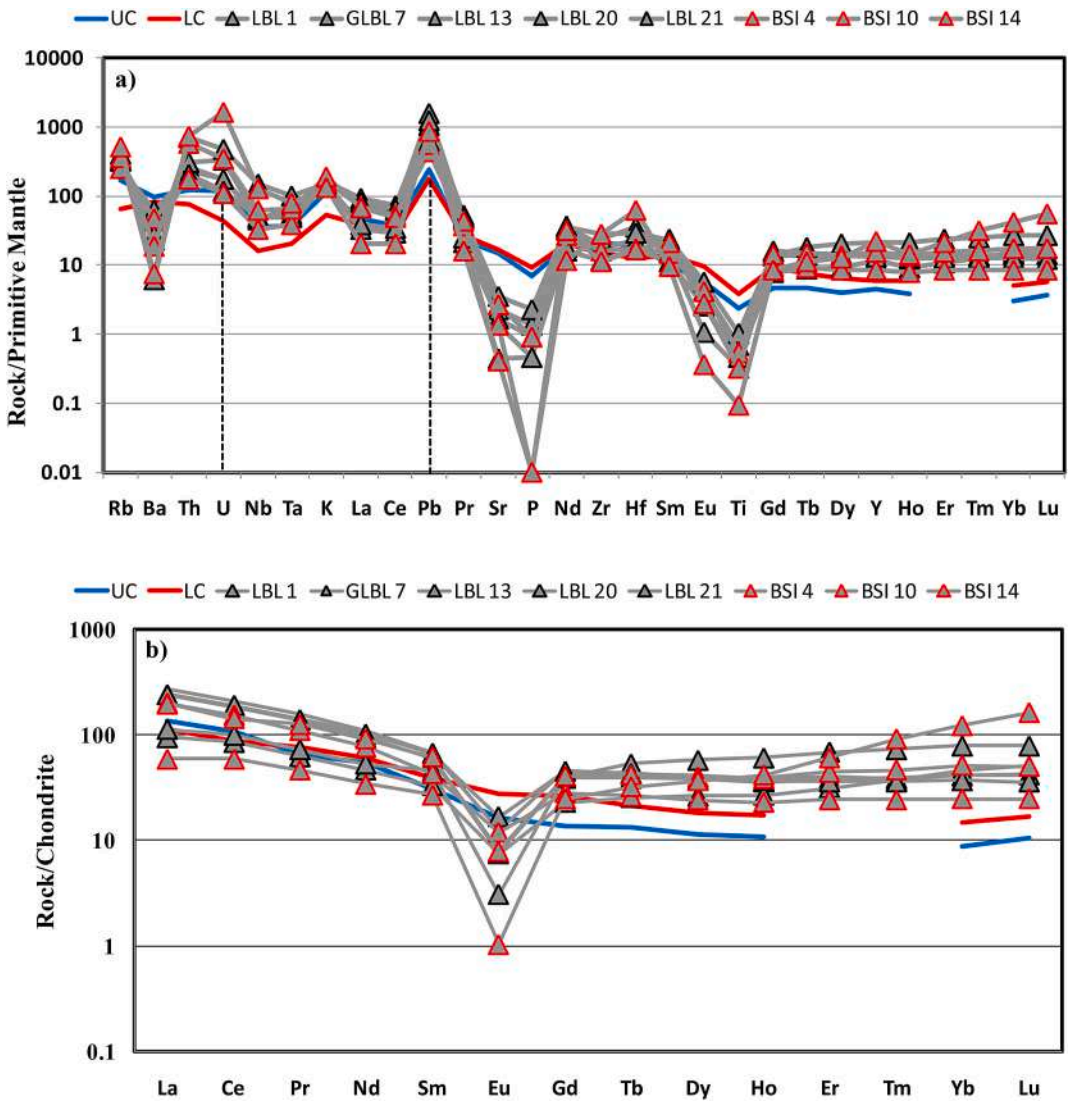

Fig. 10. (a,b) Primitive mantle-normalized trace element spider diagrams and corresponding chondrite–normalized REE patterns of the studied biotite granite from Lombel and Badesi massifs. Normalization factors are after Sun and McDonough (1989).

of a post-collisional magmatic event that extended across central Gondwana (e.g., Penaye et al., 2006; Isseini et al., 2012; Dawaï et al., 2013; Shellnutt et al., 2015, 2017, 2018; Basua et al., 2022, Fig. 11). The estimated 10K*Ga/Al (3.1–3.6) and R1 (2300–2600) are within the limit for the post–orogenic A–type granites (Sylvester, 1989; Dawei et al., 1996, Fig. 12a and b). Such post–collisional signatures (Fig. 12c) of this granite are noted by high Y/Nb ratio (> 1.2) and elemental values in the Rb vs. Ta+Yb and Nb vs. Y diagrams of Pearce et al. (1984) (Fig. 12d), this is consistent with the diagrams of Batchelor and Bowden (1985) and Maniar and Piccoli (1989). Furthermore, the biotite compositions indicate that these rocks were emplaced in an anorogenic setting after the collisional phase.

Based on tracer radiogenic isotope reports (Sr–Nd–Hf; detailed explanation below), the studied granites indicate a predominantly mantle-derived source. Similar Nd–Hf values obtained by Yomeun et al. (2022a,b) and Almeida et al. (2023) have reported the same source. Our combined results suggest that such a mantle source might have ponded and interacted with the crust. The re-melting of this newly formed mantle–derived source within the crust would have been initiated during the transition from a collisional to an extensional tectonic environment in the central Sahara (e.g., Penaye et al., 2006; Couzinié et al., 2020; Shellnutt et al., 2021). The estimated temperatures revealed a hot marginally peraluminous magma. These temperatures correspond with the emplacement ages that occurred toward the end of the Neoproterozoic Pan–African orogeny in Cameroon (e.g., Toteu et al., 2004; Penaye et al., 2006).

Petrographically, these granites consist of K–feldspars, quartz, plagioclase, and biotite with a few accessory minerals, such as zircon, apatite, titanite, and allanite, similar to those of the alkaline granites (e.g., Eby, 1992; Bonin, 2007, Shellnutt et al., 2018; Basua et al., 2022, Fig. 5). The absence of sodic pyroxene (aegirine) is uncommon, because it has been reported in the nearby Heri alkaline biotite granite massif (~ 600 Ma; Basua et al., 2022, Fig. 2c). The studied granites of Figuil registered elevated SiO_2 (> 73 wt%), Ga/Al, FeO^T/MgO, K_2O+Na_2O, HFSE, REE, and low LILE/HFSE ratios, MgO, CaO, and Al_2O_3, which are considered diagnostic features of A–type granites (e.g., Collins et al., 1982; Whalen et al., 1987; Bonin, 2007).

The biotite chemistry shows a near–annite composition (Fig. 6a), which suggests magmatic conditions that favor an increase in the Fe/(Fe+Mg) ratio and total FeO. Such a composition is associated with the anorogenic alkaline field (Fig. 6b–d). In terms of FeOt, the biotite in this work shows some similarities with those from the A–type granites studied by Shellnutt et al. (2018) and differences with those by Isseini et al. (2012) from the central Sahara (Fig. 6c and d). This observation

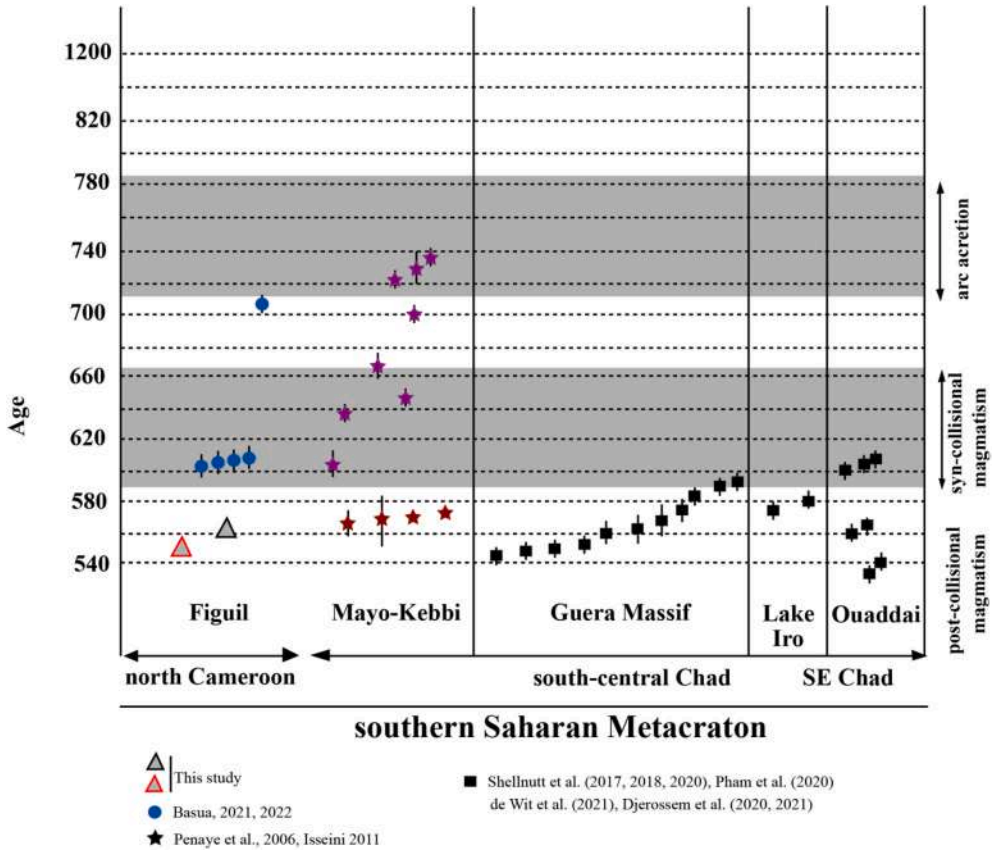

Fig. 11. Timeline correlation of the studied post–collisional granite U–Pb geochronology with those of central–south Chad of Penaye et al. (2006), Isseini (2011), Shellnutt et al. (2017, 2018, 2020), Pham et al. (2020), de Wit et al. (2021), Djerossem et al. (2020, 2021).

suggests that different magmatic conditions (e.g., oxidation, temperature, and pressure), prevailed in the study area.

The studied peraluminous, ferroan, high–K, and alkali-calcic granites (Fig. 8b–e) are indifferent to some post-collisional A–type granitoids studied in Cameroon and the nearby south-central Chad domain by Isseini et al. (2012), Pham (2018), Shellnutt et al. (2018), and Basua et al. (2022). Given that the geochemistry of the rocks from both domains (Cameroon–Chad) resemble each other, this suggests some similarities in terms of petrogenesis (degree of melting and fractional crystallization) and the nature of the source magmas.

6.2. *Formation age of the Lombel & Badesi granite & regional geological correlation*

The Figuil area and part of the south-central Chad belong to the unknown southern limit of the Sahara Metacraton (e.g., Shellnutt et al., 2015; Basua et al., 2022). Radiogenic isotope ages (U–Pb and Rb–Sr) have been reported from rock exposures sporadically distributed in the region (e.g., Isseini et al., 2012; Dawaï et al., 2013; Shellnutt et al., 2018, 2020, 2021; Basua et al., 2022) and were used to tentatively describe the tectono–magmatic evolution in this area (Fig. 11). Ages obtained by de Wit et al. (2021) enabled the classification of at least three age groups: > 1600 Ma, ~ 1000 Ma, and between 623 and 557 Ma from central Chad, consistent with the previous work of Penaye et al. (2006) in SW Chad. Note that similar ages (zircon U–Pb ~ 707, ~ 600, and 566–555 Ma; Fig. 2c) have been reported from A–type granites in Figuil–Cameroon (Basua et al., 2022), coupled with those of Dawaï et al. (2013), Li et al. (2017), and Ngatcha et al. (2022); it therefore suggests simultaneous magmatic events in both domains (Cameroon–Chad). These ages reflect the fractional crystallization and segregation of a mafic melt that probably began with the release of mafic–intermediate components and subsequently by the syn–collisional, calc–alkaline granitic batholiths (Penaye et al., 2006). This was then proceeded by post–collisional alkaline granites of < 610 Ma (Isseini et al., 2012; Shellnutt et al., 2018; Pham, 2018; Basua, 2021; Basua et al., 2022) initiated by regional deformation ~ 623–613 Ma (de Wit et al., 2021). However, for the case of the alkaline granites, one older zircon U–Pb age of 707.7 Ma reported from the Djabe massif situated at the Cameroon–Chad border (Basua et al., 2022) suggests that some massifs were emplaced before the active orogenic phase.

The registered zircon U–Pb ages of 566 ± 2.5 Ma (Lombel; Figs. 7c) and 555 ± 2.7 Ma (Badesi; Fig. 7d) confirm post–collisional magmatism in Babouri–Figuil. These ages are similar to those reported in previous studies by Isseini et al. (2012), Shellnutt et al. (2018), Pham (2018), Basua (2021), and de Wit et al. (2021). The undeformed nature of these granites supports their post–collisional origin (Fig. 5). Moreover, these ages fall within the limits of the "younger" (< 570–500 Ma), post–collisional granitoids in Cameroon, south–central Chad, and the Central Africa Republic (e.g., Toteu et al., 2004; Penaye et al., 2006; Shellnutt et al., 2018; de Wit et al., 2021). This suggests widespread post-magmatism in the southern Sahara Metacraton. The fact that the various magmatic activities of the studied massifs occurred < 11 Ma might indicate that a prominent large post–orogenic reservoir had once existed that initiated these plutons at relatively shorter intervals (Basua et al., 2022).

Three other age groups, 1054 ± 139 Ma, 602 ± 11.8–582 ± 6.1 Ma, and < 540 Ma, were obtained from the Lombel and Badesi massifs, which are considered as unclassified zircon crystals. For instance, the 1054 ± 139 Ma (Stenian–Tonian) is probably an inherited core extracted from the surrounding rock. A similar inherited $^{206}Pb/^{238}U$ age of 1039 ± 24 Ma was reported for the Guéra massif in the South–Central Chad by Shellnutt et al. (2020). A similar age has also been reported for

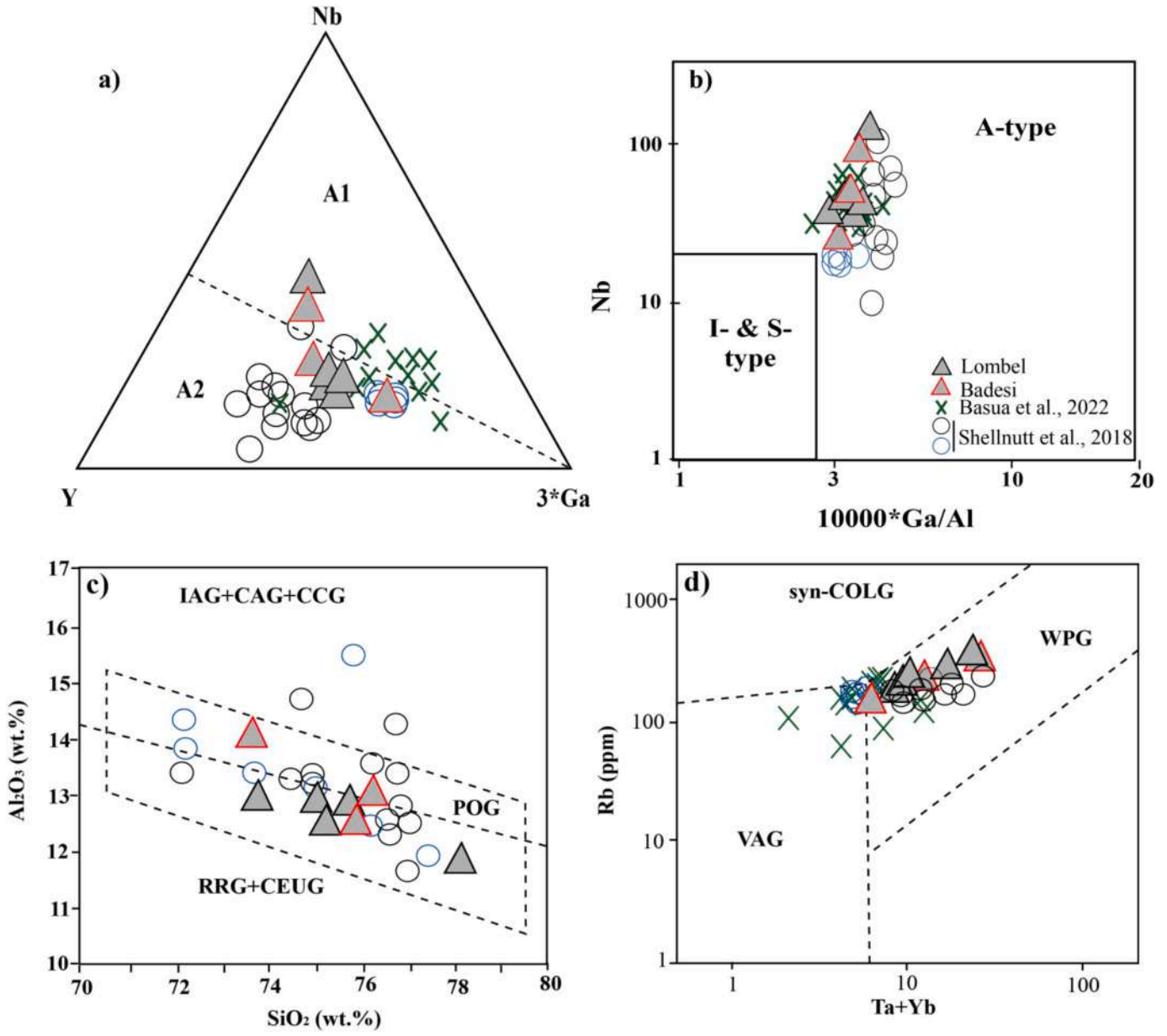

Fig. 12. Binary and ternary discrimination plots for the studied A-type granite: (a) Y–Nb–3*Ga (Eby, 1992), (b) 10,000 × Ga/Al vs. Nb (ppm) (Whalen et al., 1987), (c) SiO_2 (wt%) versus Al_2O_3 (wt%) (Maniar and Piccoli, 1989), (d) Ta + Yb versus Rb (ppm) (Pearce et al., 1984). Triangle plots = this study and circle plots = Shellnutt et al. (2018).

an I–type anatectic granite in the Mamfe Basin belonging to the CAOB (Kanouo et al., 2021b). Thus, it is suggested that the magma that generated the Badesi biotite granite, where the ~ 1054 Ma inherited zircon was extracted, probably interacted with an older crust (e.g., Paleoproterozoic; Penaye et al., 2006; Shellnutt et al., 2018; Basua et al., 2022) during ascent to a shallower depth.

The second inherited zircon age group (early Ediacaran) is similar to the emplacement ages of some known granitic massifs in this area, for example, volcanic–arc granite of the Guéra Massif in south–central Chad (~ 590 Ma; Shellnutt et al., 2020) and syn- to late-post collisional A–type granites from Figuil (Basua et al., 2022, Fig. 2c). As per Shellnutt et al. (2020), post–collisional magmatism (~ 590 Ma) continued in the eastern regions of Chad after the collision occurred (≥ 610 Ma) in the west (Cameroon). Thus, these inherited zircons were probably extracted from the granitic rock formed during a subducting event in a back–arc setting, as is the case of Babouri–Figuil.

Younger unclassified ages (< 555 Ma) were obtained from zircon crystals with diverse physical and chemical differences. This possibly indicates registered post-emplacement events that reset the initial timing of the zircon. This can be attributed to Pb mobilization by late hydrous fluids after emplacement (Rolf and Write, 1993). However, the lack of sufficient evidence did not permit us to discuss this set of ages further.

6.3. *Petrogenesis of the Babouri–Figuil granite*

6.3.1. *Fractional crystallization*

The studied samples displayed correlations in the Harker variation diagrams (Fig. 9). Ba, Sr, and Eu are strongly depleted, reflecting the fractionation of plagioclase from the parental magma (Fig. 10a). Negative correlations between either TiO_2 or Fe_2O_3 and SiO_2 coupled with negative P and Ti anomalies indicate apatite and Fe–Ti oxide fractionation (Karsli et al., 2012). These accessory mineral phases potentially influenced the distribution of HFSE and REE. The Ti (mol/100 g) *vs.*

maficity correlation could be interpreted as an indication of peritectic assemblage entrainment related to partial melting (Clemens and Stevens, 2012; Sup. 1).

The observed strong negative Eu anomalies indicate that fractionation of feldspar or residual feldspar in the source played a significant role in the petrogenesis of this granite (Dahlquist et al., 2010; Fig. 10b). Our samples have low Sr/Y and La_N/Yb_N ratios and strong negative Eu anomalies, implying petrogenesis that mainly involves plagioclase, with garnet and amphibole absent or playing a minor role (Collins et al., 1982; Table 5). This is supported by the relatively constant REE patterns of the massifs, indicating low–pressure melting and differentiation (Dahlquist et al., 2010).

Comparatively, the trace and rare earth element patterns of these mantle–derived granites show some similarities with the upper and lower continental crusts, which possibly suggest crustal contamination or mixing from both sources (Fig. 10). In addition, their elemental ratios, such as Nb/U and K/U, are consistent with the average middle and lower (Nb/U < 10, Ta/U = 0.5, Ce/Pb = 3.9, Th/La = 4.3 and K/U < 15; Rudnick and Gao, 2003) crustal geochemistry (Table 2).

The systematic depletion of HFSE, such as Ta, Nb, and Ti (Fig. 8), and the strong enrichment of Pb in all samples suggest inherited features from a source that was involved in arc formation. Moderately depleted Nd isotopes indicate that arc magmatism (with mantle–derived melt) continued after the collision and closure of the arc. This mantle input was possible during crustal extension. Therefore, a mixed K–rich source and mantle–derived melt gave these granites a high–K composition, high SiO_2, and moderately depleted initial Nd isotopes.

6.3.2. *Biotite & whole–rock compositions: magmatic conditions*

The mineralogy of the Lombel and Badesi granites (plagioclase, K–feldspars, quartz, biotite, apatite, and Fe–Ti oxides) has been considered to constrain various magmatic conditions in each system. The chemical composition of the biotite indicates primary magmatic biotites (Fig. 13a) with minor alteration to chlorite (Fig. 5i). Reliable temperatures based on sensitivity and the coupled exchange of Ti and Fe^{2+} in biotite from 613 to 647 °C were estimated using the equation of Luhr et al. (1984). These temperatures are similar to those obtained from the Guera massif in south–central Chad by Pham et al. (2020) (Fig. 13b).

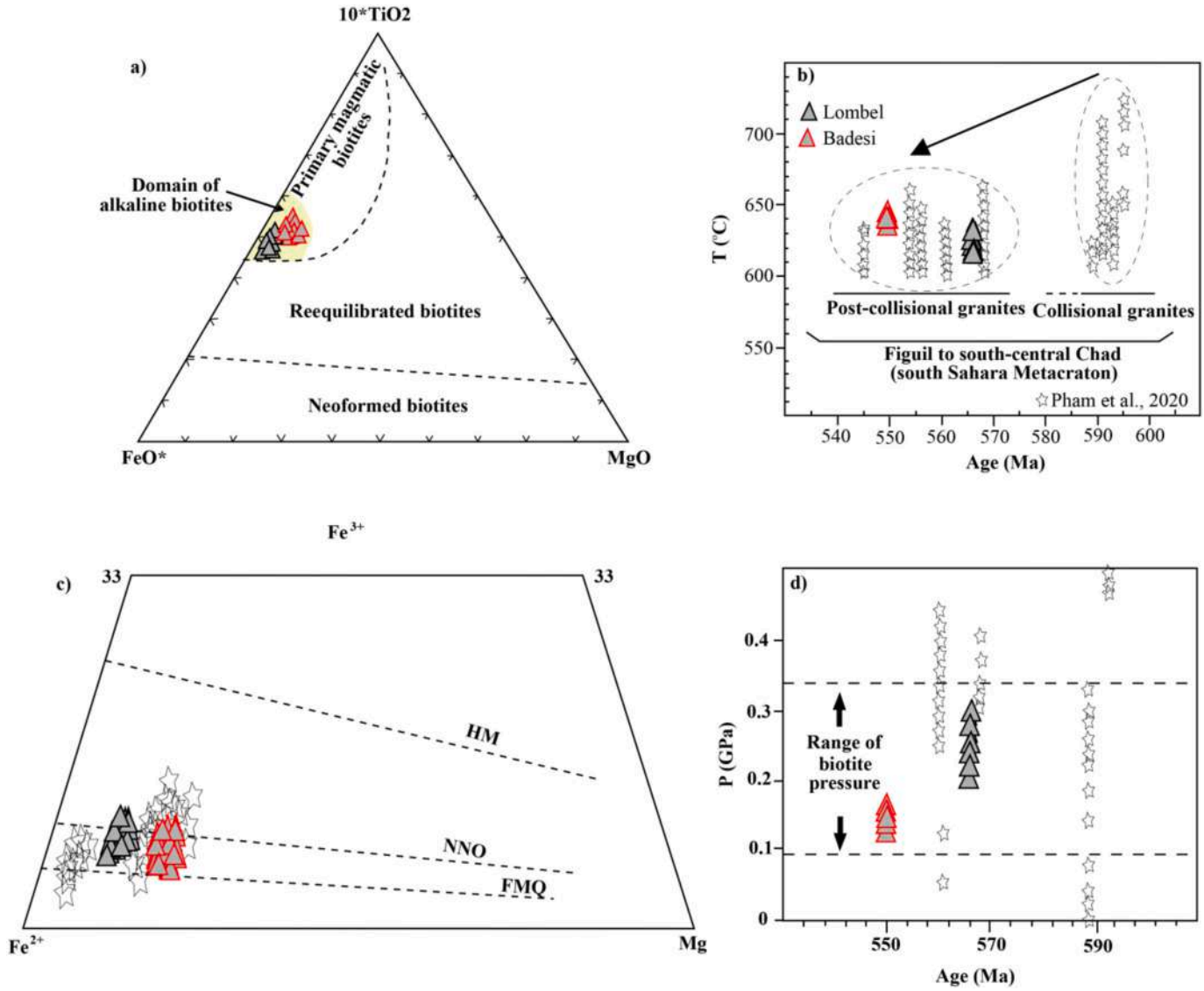

Fig. 13. Ternary and binary plots of the studied granites (a) FeO*-10 × TiO_2–MgO indicating primary magmatic biotite, Nachit et al. (2005); (b) biotite crystallization temperature variations with respect to the crystallization ages of the studied granites compared with those of central-south Chad (Pham et al., 2020); (c) plot of biotite redox conditions of the studied granites compared with those of Pham et al. (2020); (d) biotite crystallization pressure variations with respect to the crystallization ages of the studied granites compared with those of central-south Chad (Pham et al., 2020). The redox buffers of Eugster and Wones (1962) are HM = hematite-magnetite; NNO=Ni–NiO; QFM = quartz–fayalite-magnetite.

However, high and unreliable values from 781 to 904 °C were calculated from the whole–rock Zr compositions (Table 7). In south-central Chad, the biotite temperatures decreased from collisional to post-collisional granites (Fig. 13b). However, our results show that the older Lombel massif had recorded lower temperatures (566 Ma; 613–633 °C) relative to the younger Badesi massif (550 Ma; 633–647 °C) (Fig. 13b). This observation may suggest temperature unbalance within the post–collisional granites of the central Sahara. Nonetheless, the biotite temperatures overlap with those of the post–collisional granite and contrast with those of the collisional granites from the Guéra massif and Lake Fitri inliers (Pham et al., 2020). The estimated biotite temperatures suggest that the Lombel and Badesi massifs crystallized from fairly hot magma (Table 2). These temperatures fixed the oxidation reaction of the studied granites with a buffer of pure quartz–fayalite–magnetite ΔQFM = −0.6 (Fig. 13c; Sup. 2). In this study, the biotite crystallization pressures were estimated based on the concentration of TiO_2 2.89–3.77 and Al^{VI} 0–0.36 that are linked to the emplacement depth of their host plutons. The low-temperature massif (Lombel) registered the highest crystallization pressures from 200 to 280 MPa; in contrast, the high–temperature massif (Badesi) recorded lower restricted values from 120 to 160 MPa (Fig. 13d). The values calibrate a biotite–geobarometer and provide valuable insight into the thermal history and crystallization conditions of the studied granites. These resemble those from the south-central Chad and fall within the range of biotite pressure in the Age (Ma) vs. P (GPa) diagram (Fig. 13d). The crystallization pressures and water content (H_2O, 3.0–3.5 wt%; Table 2) from biotite, coupled with the emplacement depth < 15 km from whole rock compositions (Table 7), are consistent with reduced conditions, and shallow crustal emplacement levels, respectively.

These results are consistent with reduced A–type granites confirmed by low molar ferric-ferrous iron oxide ratios $Fe^{3+}\# = 0.2$ (Yang et al., 2021). $Fe^{3+}\# = 0.1$ reflects a much-reduced condition, whereas $Fe^{3+}\# = 1.0$ indicates the most oxidizing condition (Yang et al., 2021; Table 7). The calculated biotite water contents of ~ 3.0–3.5 wt% (Table 2) suggest that the studied Babouri–Figuil granite was generated presumably from a H_2O–poor protolith with decreasing H_2O solubility at low pressure (Eby, 1992; Patino Douce, 1997).

6.3.3. *Source nature of magma*

The source of A–type granite can be traced either from the crust or mantle or from a mixed source (e.g., Collins et al., 1982; Eby, 1992; Bonin, 2007). The first inference drawn from our data is that both massifs display trace element patterns similar to the crust (Fig. 10). This may be due to contamination with the crust or extreme fractional crystallization of the mantle melt, confirmed by high $SiO_2 > 70$ wt % and very low contents of MgO < 1 wt%, Mg# < 20 %. Additionally, isotopic pairs of Nd–Sm, Lu–Hf, and Sr–Rb shed more light on the generic sources of these granites, as further discussed below.

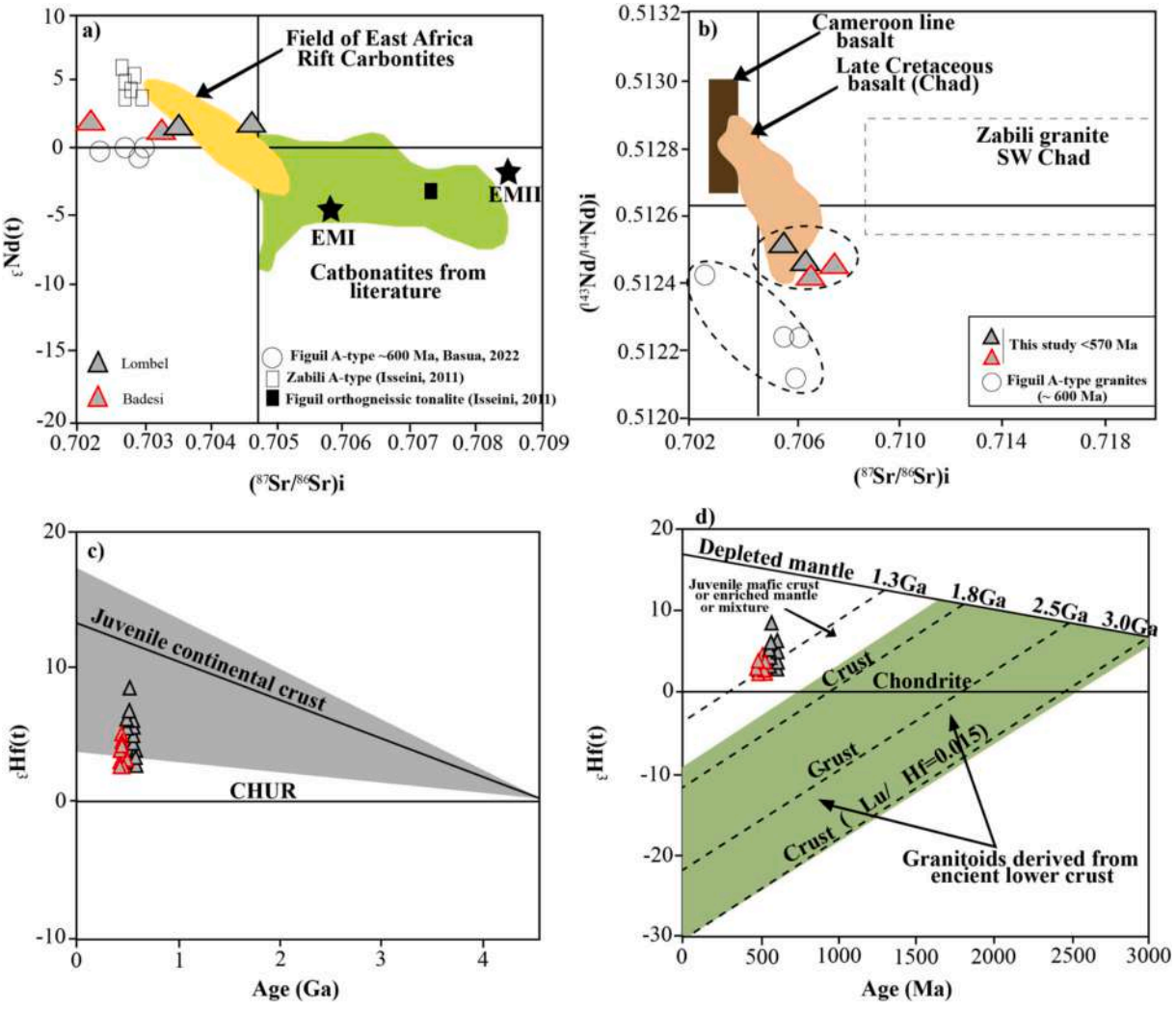

Fig. 14. Source discrimination plots of the studied granite from Lombel and Badesi massifs: (a) $\varepsilon_{Nd}(t)$ versus $(^{87}Sr/^{86}Sr)i$; (b) $(^{87}Sr/^{86}Sr)i$ versus $(^{143}Nd/^{144}Nd)i$; (c) Age (Ga) versus $\varepsilon_{Hf}(t)$; (d) Age (Ma) versus $\varepsilon_{Hf}(t)$.

Strontium concentration in silicic crust is relatively high. This indicates that mantle melt that interacted with such crust would normally yield higher initial Sr values. Conversely, the studied granite samples yielded low to moderate initial Sr isotopic values Sr(i) = 0.70212–0.70458 (Fig. 14a and b; Table 6), which reflects mainly a mantle contribution for this granite. Besides, the samples were more enriched in Nd (36.1–48.0 ppm) than in Sm (6.6–10.3 ppm) (Table 6) and yielded $^{176}Hf/^{177}Hf = 0.282547–0.282711$ and $^{176}Yb/^{177}Hf < 0.1$, resembling mantle values. These values also suggest that the depleted–mantle source of this granite was chemically enriched by metasomatized fluid and melt from a subducted crust (e.g., Liégeois and Stern, 2010).

Samples from both massifs yielded moderate to depleted initial Hf values [$\varepsilon_{Hf}(t) = +2.63$ to $+8.40$] and moderately depleted initial Nd values [$\varepsilon_{Nd}(t) = +1.26$ to $+2.10$]. These values resemble those of the mantle–derived components as suggested by Yomeun et al. (2022a,b) and Almeida et al. (2023). The initial Hf values show a wide range and plot in the juvenile crust field (Fig. 14c), whereas the initial Nd value resembles the CHUR and almost plots in the Pan–African basement rock field (Fig. 14d). The combined Nd–Hf–Sr data suggest a depleted mantle source and are similar to the post–collisional granites reported in the southern Saharan Metacraton. Alternatively, this presumably reflects a short–lived juvenile crust extracted from the mantle. This conjecture comes from the slightly enriched initial Nd isotopic values of the studied rocks, coupled with the few geochemical parameters already mentioned. Nd *vs.* Sr values plot near to the late Cretaceous basalts of SW Chad indicating geochemical resemblance (Fig. 14b).

Comparatively, our values are slightly higher than those obtained from syn- to early post-collisional ferroan granites [600 Ma; $\varepsilon_{Nd}(t) = -2.5$ to -0.3] in the same locality attributed to crust–mantle sources (Basua, 2021; Basua et al., 2022, Fig. 14a and b). The obtained values overlap with the post–collisional A–type granites in south–central Chad studied by Shellnutt et al. [2018; $\varepsilon_{Nd}(t) = +1.3$ to $+2.9$] and Isseini et al. (2012) [$\varepsilon_{Nd}(t) = +1.6$ to $+7.0$] a few km east of the study area. This suggests regional post–Neoproterozoic magmatism between the Babouri–Figuil and SW Chad domains. Shellnutt et al. (2018) attributed their obtained values to a mantle source, whereas the wide-spread and moderately depleted values obtained from ferroan granite in the Zabili massif (567 ± 10; Isseini et al., 2012) were ascribed to a juvenile source or the melting of a crustal protolith.

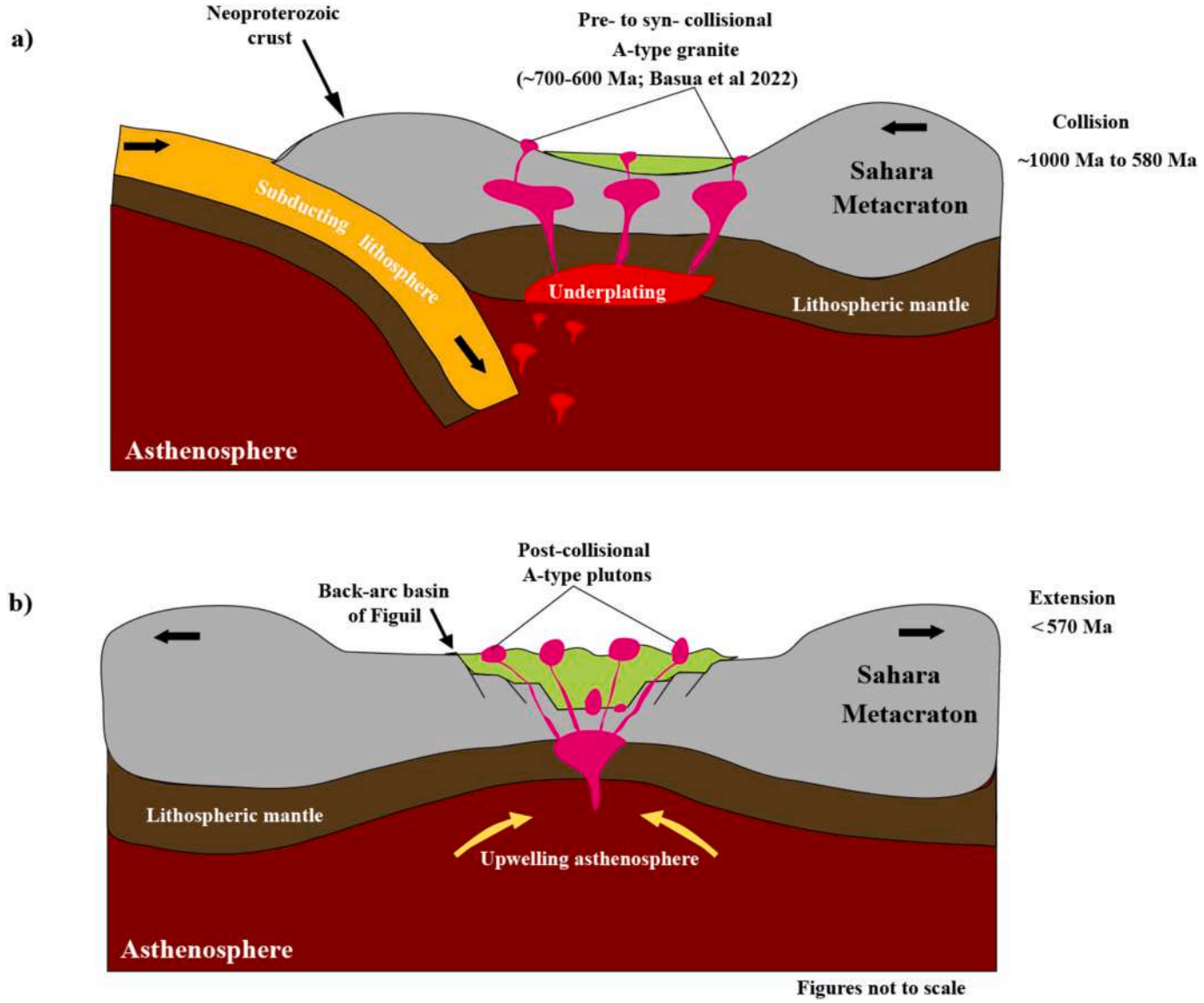

Fig. 15. Simplified tectonic models of the Babouri–Figuil magmatic complex depicting (a) collisional phase tectonic between the West Africa craton and the Sahara Metacraton ~ 600 Ma; (b) extensional phase tectonic environment in a within plate setting after recycling of subducted oceanic crust prior to ~ 570 Ma.

6.4. Lithotectonic evolution of the south–central Saharan Metacraton

From geochronologic, geochemical, and petrographic analyses, it is apparent that the south–central Saharan Metacraton has undergone a complex tectonomagmatic evolution. For example, radiogenic ages from these areas suggest more than one tectonic regime linked to Gondwana pre–drift > 1000 Ma, followed by subduction of microplates and subsequent collisions coupled with regional deformations and magmatism (Fig. 11). At least two deformation phases, ~1000 and ~600 Ma, might have influenced the lithotectonic units in this area. Age data by de Wit et al. (2021) (> 1600, 1000, and 623–557 Ma) and Penaye et al. (2006; 737–723, 665–570 and < 570 Ma) support three main magmatic episodes. Further studies by Isseini (2011) and Isseini et al. (2012), Shellnutt et al. (2017, 2018, 2019b, 2020, 2021), Pham (2018), Djerossem et al. (2020, 2021), Basua (2021), and Basua et al. (2022) have shed more light on the post–collisional magmatic activities in these regions (Fig. 15).

In the reconnaissance framework of the south–central Saharan Metacraton, a temporal relation or definite fractionating trend is not possible because of spatial data. Nonetheless, the few results indicate abundant magmatism between 665 and 554 Ma. The magmatic evolution began as the mafic to intermediate complexes emplaced, presumably in a magmatic arc at < 1000 Ma. This was followed by the emplacement of syn–collisional granitoids (e.g., Mayo-Kebbi batholiths) and subsequently by post–tectonic alkaline granitoids (e.g., Penaye et al., 2006; Djerossem et al., 2020; Shellnutt et al., 2020, 2021; de Wit et al., 2021). Studies indicate that majority of the rocks that crop out in the south–central Saharan Metacraton are high–K calc–alkaline to shoshonitic, suggesting the involvement of crustal and K–rich sources, consistent with high SiO_2 (> 66%) and moderately enriched initial Nd isotopic data (e.g., Djerossem et al., 2020; de Wit et al., 2021). These compositions plot close to those of the peralkaline and metaluminous fields. However, a few mafic to intermediate rocks are tholeiitic; a few samples show depleted HFSE, whereas others do not in the multi-element distribution diagrams reflecting variable mantle–derived sources. Granitoids are frequently characterized by the depletion of Nb, Ta, and Ti, with strong to moderate depletion of Ba, Sr, P, and Eu, depicting arc-like petrogenesis and attest K–feldspar, plagioclase, and apatite fractionation.

The distributions of HFSE and REE in high–SiO_2 granitoids were potentially affected by accessory phases. Most rock types from the south–central Saharan Metacraton are Pb-enriched, indicating that crustal materials influenced their mantle–derived origin. A small proportion of potential adakitic rocks was suggested by de Wit et al. (2021), who also observed adakitic features in samples studied by Shellnutt et al. (2020) in Guéra and by Djerossem et al. (2020) in southern Ouaddai. Therefore, the presence of adakite suggests the existence of thick (> 30 km; garnet stable) and thin (< 30 km; plagioclase stable) crusts in the south–central Saharan Metacraton (Fig. 15a and b). According to de Wit et al. (2021), a thick crust occurred in a continental arc at ~ 600 Ma. Similar rocks within the CAOB have been attributed to the partial melting of Archean TTG (Tchakounte et al., 2017). Deformation features were observed mostly in rocks emplaced before ~ 610 Ma, consistent with syn–collision magmatism, in contrast to their post–collision counterparts.

In summary, Figuil should be considered part of the south–central Saharan Metacraton and the northern segment of the CAOB. The study area, which is largely dominated by Neoproterozoic upper crust, was intruded into a Mesoproterozoic basement. Magmatism possibly occurred in separate episodes across different tectonic settings from ~ 1060 to 557 Ma. The last deformation occurred within a relatively short period (~ 10 Ma, between 623 and 613 Ma), after which post–collisional granite magmatism continued at < 557 Ma. Our studied granites are among the youngest post–collision rocks, and the obtained ages presumably indicate the end of the Pan–African orogeny within the central Sahara Metacraton. They are similar to those reported in the Chad and Central Africa Republic, suggesting regional magmatism (e.g., Penaye et al., 2006; Isseini et al., 2012; Shellnutt et al., 2017, 2018, 2019, 2020, 2021; Djerossem et al., 2020; Basua, 2021; de Wit et al., 2021; Basua et al., 2022). This area has undoubtedly evolved from a magmatic arc to subduction with the closure of a Paleo–Ocean, accompanied by a series of subsequent collisions (Fig. 15a). It was terminated by lithospheric delamination, leading to crustal extension with corresponding thinning and post–collisional magmatism, with exhumation and regional peneplanation at ~ 550–500 Ma (de Wit et al., 2021) (Fig. 15b).

7. Conclusions

Studies based on petrology, mineral chemistry of biotite, lithogeochemistry, U-Pb geochronology, and various tracer radiogenic isotopes were used to characterize the granites from Babouri–Figuil; the results suggest the following conclusions:

1. The identification of late Ediacaran post-collisional granitoids in the Lombel massif (566 ± 2.5 Ma; zircon U–Pb age) and the Badesi massif (555 ± 2 Ma; zircon U–Pb age). These ages likely marked the end of the Pan-African orogeny forming part of the Babouri-Figuil magmatic complex (Cameroon).
2. The Lombel and Badesi massifs were emplaced at upper crustal levels and had moderate crystallization temperatures (613–647 °C) and low oxygen fugacity (fO_2 ~ ΔQFM -0.6). They are geochemically similar to other reduced post-collisional A–type granites.
3. Their geochemical compositions suggest that very selective partial melting of a mantle -like source, then considerable fractional crystallization and minor crustal contamination (AFC) are the main processes responsible for generating these granites. They are related to post-collisional extensional settings, such as those of contaminated, sub-to mid–alkaline, ferroan, high–K, alkalic–calcic, and marginally peraluminous alkali granites located in the same terrain.
4. From the contrasting isotopic Hf–Nd–Sr signatures, we propose that the massifs were either linked to a mantle–derived source or possibly originated from a relatively juvenile continental crust accreted before 570 Ma.
5. The reactivation of major fractures (for example, the N–S oriented Guider–Sorawel Shear Zone) possibly induced the ascent of these mantle-derived melts with AFC processes into the shallow crust.

The unclassified older inherited zircon (1054 Ma) was presumably from the old Mesoproterozoic crust and incorporated into the post-collisional granite during AFC processes during emplacement. The early Ediacaran–inherited zircons possibly indicate interaction with a volcanic–arc-like granitic protolith, whereas dates < 550 Ma suggest Pb mobilization by hydrous fluids.

CRediT authorship contribution statement

Basua Afanga Archelaus Emmanuel: Writing – review & editing, Writing – original draft, Investigation, Data curation, Conceptualization. **Changqian Ma:** Funding acquisition. **Kanouo Sylvestre Nguo:** Resources, Formal analysis. **Lian-Xun Wang:** Funding acquisition, Formal analysis. **David R. Lentz:** Validation, Resources. **Soumyajit Mukherjee:** Validation, Resources, Funding acquisition. **Bovari Yomeun Syprien:** Methodology. **Yu-Xiang Zhu:** Software. **Nformidah Ndah Siggy Signe:** Data curation.

Declaration of competing interest

The authors declare that they have no conflicts of interest.

Data availability

Data will be made available on request.

Acknowledgements

The first author was supported by the National Natural Science Foundation of China (Grant No. 41972066) and the Ministry of Education's Belt and Road Intelligence Project on Education, Science, Culture, and Health (No. DL20180059). A CPDA Grant (IIT Bombay) supported SM. The authors sincerely appreciate the Editor–in–Chief Prof. Mohamed G Abdelsalam for the editorial handling of this manuscript. The reviewers, G. Shellnutt and Samuel Nunoo, comments and suggestions were important and have significantly improved this contribution. A sub-divisional officer (DO) of Figuil and local chiefs permitted this work.

Appendix A. Supplementary data

Supplementary data to this article can be found online at https://doi.org/10.1016/j.jafrearsci.2024.105212.

References

Abdelsalam, M.G., Liégeois, J.-P., Stern, R.J., 2002. The Saharan metacraton. J. Afr. Earth Sci. 34 (3–4), 119–136.

Abdelsalam, M.G., Gao, S.S., Liégeois, J.-P., 2011. Upper mantle structure of the SaharanMetacraton. J. Afr. Earth Sci. 60 (5), 328–336. https://doi.org/10.1016/j.jafrearsci.2011.03.009.

Almeida, M.E., Macambira, M.J.B., Araújo Mendes, Túlio Amós de, Orestes, J.S., dos Santos, 2023. Post-collisional 1.75 Ga mantle-derived felsic magmatism in the Cauaburi orogeny, NW Amazon craton, Brazil. JGSB 6, 217–237.

Basua, A.A.E., 2021. Geochronology and Petrogenesis of the Pan-African A-type Granitoids from the Babouri-Figuil Complex, NW Cameroon Domain: Implication for the Tectonic Evolution of the Central Africa. Unpublished Ph.D. Thesis, China University of Geosciences, Wuhan, p. 260.

Basua, A.A.E., Ma, C., Nguo, K.S., Wang, L.-X., Lentz, D.R., Mukherjee, S., Nformidah-Ndah, S.S., Yomeun, B.S., 2022. Petrogenesis and tectonic setting of A-type granites in the Babouri-Figuil Magmatic Complex (North Cameroon): constraints from whole rock geochemistry, zircon UPb geochronology and Sr-Nd-Hfisotopes. Lithos 414, 106618.

Batchelor, R.A., Bowden, P., 1985. Petrogenetic interpretation of granitoid rock series using multicationic parameters. Chem. Geol. 48 (1–4), 43–55.

Begg, G.C., Griffin, W.L., Natapov, L.M., O'Reilly, S.Y., Grand, S.P., O'Neill, C.J., et al., 2009. The lithospheric architecture of Africa: seismic tomography, mantle petrology, and tectonic evolution. Geosphere 5 (1), 23–50. https://doi.org/10.1130/ges00179.1ZHUETAL.10.1029/2019RG00068964of84.

Bonin, B., 2007. A-type granites and related rocks: evolution of a concept, problems and prospects. Lithos 97, 1–29.

Bouvier, A., Vervoort, J.D., Patchett, J., 2008. The Lu-Hf and Sm-Nd isotopic composition of CHUR: constraints from unequilibrated chondrites and implications for the bulk composition of terrestrial planets. Earth Planet Sci. Lett. 273, 48–57.

Clemens, J., Stevens, G., 2012. What controls chemical variation in granitic magmas? Lithos 134, 317–329.

Collins, W.J., Beams, S.D., White, A.J.R., Chappell, B.W., 1982. Nature and origin of A-type granites with particular reference to southeastern Australia. Contrib. Mineral. Petrol. 80, 189–200.

Couzinié, S., Ménot, R.P., Doumnang, J.C., Paquette, J.L., Rochette, P., Quesnel, Y., Deschamps, P., Ménot, G., 2020. Crystalline inliers near lake Iro (SE Chad): post-collisional Ediacaran A2-type granitic magmatism at the southern margin of the saharan metacraton. J. Afr. Earth Sci. 172, 103960 https://doi.org/10.1016/j.afrearsci.2020.103960.

Dahlquist, J.A., Alasino, P.H., Eby, G.N., Galindo, C., Casquet, C., 2010. Fault controlled Carboniferous A-type magmatism in the proto-Andean foreland (Sierras Pampeanas, Argentina): geochemical constraints and petrogenesis. Lithos 115 (1–4), 65–81.

Dawaï, D., Bouchez, J.-L., Paquette, J.-L., Tchameni, R., 2013. The Pan-African quartz-syenite of Guider (north-Cameroon): magnetic fabric and U–Pb dating of a late-orogenic emplacement. Precambrian Res. 236, 132–144.

Dawei, H., Shiguang, W., Baofu, H., Manyuan, J., 1996. Post-orogenic alkaline granites from China and comparisons with anorogenic alkaline granites elsewhere. J. Southeast Asian Earth Sci. 13, 13–27.

De la Roche, H.D., Leterrier, J.T., Grandclaude, P., Marchal, M., 1980. A classification of volcanic and plutonic rocks using R1, R2 diagram and major-element analyses- its relationships with current nomenclature. Chem. Geol. 29 (1–4), 183–210.

de Wit, M., Bowring, S., Buchwaldt, R., Dudas, F.Ö., MacPhee, D., Tagne-Kamga, G., Dunn, N., Salet, A.M., Nambatingar, D., 2021. Geochemical reconnaissance of the Guéra and Ouaddaï massifs in Chad: evolution of proterozoic crust in the central Sahara Shield. S. Afr. J. Geol. 124 (2), 353–382.

Deer, W.A., Howie, R.A., Zussman, J., 1992. Rock-forming Minerals. 2ed. Longmans, London, p. 696.

Djerossem, F., Berger, J., Vanderhaeghe, O., Isseini, M., Ganne, J., Zeh, A., 2020. Neoproterozoic magmatic evolution of the southern Ouaddaï Massif (Chad). Bull. Soc. Geol. Fr. 191, 34. https://doi.org/10.1051/bsgf/2020032.

Djerossem, F., Zeh, A., Isseini, M., Vanderhaeghe, O., Berger, J., Ganne, J., 2021. U-Pb-Hf isotopic systematics of zircons from granites and metasediments of southern Ouaddaï (Chad), implications for crustal evolution and provenance in the Central African Orogenic Belt. Precambrian Res. 361, 106233 https://doi.org/10.1016/j.precamres.2021.106233.

Eby, G.N., 1992. Chemical subdivision of the A-type granitoids: petrogenetic and tectonic implications. Geology 20, 641–644.

Eugster, H.P., Wones, D.R., 1962. Stability reactions of the ferruginous biotite, annite. J. Petrol. 3, 82–125. https://doi.org/10.1093/petrology/3.1.82.

Frost, B.R., Barnes, C.G., Collins, W.J., Arculus, R.J., Ellis, D.J., Frost, C.D., 2001. A geochemical classification for granitic rocks. J. Petrol. 42, 2033–2048.

Frost, C.D., Da Prat, F.A., 2021. Petrogenetic and tectonic interpretation of strongly peraluminous granitic rocks and their significance in the Archean rock record. The American Mineralogist 106, 1195–1208.

Griffin, W.L., Pearson, N.J., Belousova, E., Jackson, S.E., van Achterbergh, E., O'Reilly, S.Y., Shee, S.R., 2000. The Hf isotope composition of cratonic mantle: LAM-MC-ICPMS analysis of zircon megacrysts in kimberlites. Geochem. Cosmochim. Acta 64, 133–147.

Guiraud, R., Maurin, J.C., 1992. Early cretaceous rifts of western and central Africa: an overview. Tectonophysics 213, 153–168.

Hu, Z.C., Zhang, W., Liu, Y.S., Gao, S., Li, M., Zong, K.Q., Chen, H.H., Hu, S.H., 2015. Wave signal-smoothing and mercury-removing device for laser ablation quadrupole and multiple collector ICPMS analysis: application to lead isotope analysis. Anal. Chem. 87 (2), 1152–1157.

Isseini, M., 2011. Crustal Growth and Differentiation during the Neoproterozoic Example of the Pan-African Domain of Mayo Kebbi in Southwestern Chad, Unpublished. PhD Thesis. University Henri Poincaré, Nancy, France.

Isseini, M., Andre-Mayer, A.-S., Vanderhaeghe, O., Barbey, P., Deloule, E., 2012. A-type granites from the Pan-African orogenic belt in southwestern Chad constrained using geochemistry, Sr-Nd isotopes and U-Pb geochronology. Lithos 153, 39–52.

Kamani, M.K., Wang, W., Tchouankoue, J.-P., Huang, S.-F., Yomeun, B., Xue, E.-K., Lu, G.-M., 2021. Neoproterozoic syn-collision magmatism in the Nkondjock region at the northern border of the Congo craton in Cameroon: geodynamic implications for the Central African orogenic belt. Precambrian Res. 353, 106015.

Kanouo, N.S., Lentz, D.R., Zaw, K., Makoundi, C., Basua, E.A.A., Yongué, R.F., Njonfang, E., 2021. New insights into pre-to-post ediacaran zircon fingerprinting of the Mamfe PanAfrican basement, SW Cameroon: a possible link with rocks in SE Nigeria and the Borborema Province of NE Brazil. Minerals 11 (9), 943.

Kanouo, S.N., Kouské, P.A., Lentz, D.R., Yongue, F.R., 2021b. New insights into Neoproterozoic–Cretaceous events in the Mamfe Basin (SW Cameroon, Central Africa): evidence from textural analyses, U-Th composition, and U-Pb Zircon geochronology from granitic basement. J. Earth Sci. 32 6, 1472–1484.

Karsli, O., Caran, S., Dokuz, A., Çoban, H., Chen, B., Kandemir, R., 2012. A-type granitoids from the Eastern Pontides, NE Turkey: records for generation of hybrid A-type rocks in a subduction-related environment. Tectonophysics 530, 208–224.

Kemp, A.I.S., Hawkesworth, C.J., 2003. Granitic perspectives on the generation and secular evolution of the continental crust. In: Rudnick, R.L. (Ed.), Treatise on Geochemistry, The Crust, vol. 3. Elsevier, Amsterdam, pp. 349–410.

Kennedy, W.Q., 1964. The structural differentiation of Africa in the Pan-African (±500 my) tectonic episode. Annual Reports of the Institute of African Geology 8, 48–49.

Kroner, A., 1977. Precambrian mobile belts of southern and eastern Africa – ancient sutures or sites of ensialic mobility? A case for crustal evolution towards plate tectonics. Tectonophysics 40, 101–135.

Kroner, A., Stern, R.J., 2004. Pan-African Orogeny: Encyclopedia of Geology, vol. 1. Elsevier, Amsterdam, pp. 1–12.

Le Maitre, R.W., 1989. A Classification of Igneous Rocks and Glossary of Terms: Recommendations of the IUGS Subcommission on the Systematics of Igneous Rocks. Blackwell, Oxford, pp. 130–171.

Li, X.-H., Chen, Y., Tchouankoue, J.P., Liu, C.-Z., Li, J., Ling, X.-X., Tang, G.-Q., Liu, Y., 2017. Improving geochronological framework of the Pan-African orogeny in Cameroon: new SIMS zircon and monazite U-Pb age constraints. Precambrian Res. 294, 307–321. https://doi.org/10.1016/j.precamres.2017.04.006.

Liégeois, J.-P., Stern, R.J., 2010. Sr–Nd isotopes and geochemistry of granite-gneiss complexes from the Meatiq and Hafafit domes, Eastern Desert, Egypt: no evidence for pre-Neoproterozoic crust. J. Afr. Earth Sci. 57 (1–2), 31–40.

Liu, Y., Hu, Z., Gao, S., Guenther, D., Xu, J., Gao, C., Chen, H., 2008. In situ analysis of major and trace elements of anhydrous minerals by LA-ICP-MS without applying an internal standard. Chem. Geol. 257 (1–2), 34–43. https://doi.org/10.1016/j.chemgeo.2008.08.004.

Luhr, J.F., Carmichael, I.S.E., Varekamp, J.C., 1984. The 1982 eruptions of El Chichon volcano, Chiapas, Mexico-Mineralogy petrology of the anhydrite bearing pumices. J. Volcanol. Geoth. Res. 23, 69–108. https://doi.org/10.1016/0377-0273(84)90057-x.

Ma, Q., Zheng, J.P., Griffin, W.L., Zhang, M., Tang, H.Y., Su, Y.P., Ping, X.Q., 2012. Triassic "adakitic" rocks in an extensional setting (North China): melts from the cratonic lower crust. Lithos 149, 159–173.

Maniar, P.D., Piccoli, P.M., 1989. Tectonic discrimination of granitoids. Geol. Soc. Am. Bull. 101 (5), 635–643.

Nachit, H., Abderrahmane, I., El Hassan, A., Mohcine, B.O., 2005. Discrimination between primary magmatic biotites, reequilibrated biotites and neoformed biotites. Geoscience 337, 1415–1420.

Nachit, H., Razafimahefa, N., Stussi, J.M., Carron, J.P., 1985. Composition chimique des biotites et typologie magmatique des granitoïdes. C. R. Acad. Sci. 301, 813–818.

Ngako, V., Affaton, P., Njonfang, E., 2008. Pan-African tectonics in northwestern Cameroon: implication for the history of western Gondwana. Gondwana Res. 14, 509–522.

Ngatcha, R.B., Suh, C.E., Okunlola, O.A., Nunoo, S., Ateh, K.I., Elburg, M., Hofmann, A., 2022. Crustal modelling from Pan-African granites of the Colomine Gold District, SE Cameroon: insights from zircon U-Pb dating and Lu-Hf isotope systematics. J. Afr. Earth Sci. https://doi.org/10.1016/j.jafrearsci.2021.104441.

Ngounouno, I., Déruelle, B., Guiraud, R., Vicat, P.J., 2001. Magmatismes tholéiitique et alcalin des demi-grabens crétacés de Mayo Oulo-Léré et de Babouri-Figuil (Nord du Cameroun–Sud du Tchad) en domaine d'extension continentale. C. R. Acad. Sci. Paris 333, 201–207.

Patino Douce, A.E., 1997. Generation of metaluminous A-type granites by low-pressure melting of calc-alkaline granitoids. Geology 25 (8), 743–746.

Pearce, J.A., Harris, N.B., Tindle, A.G., 1984. Trace element discrimination diagrams for the tectonic interpretation of granitic rocks. J. Petrol. 25, 956–983.

Peccerillo, A., Taylor, S.R., 1976. Geochemistry of Eocene calc-alkaline volcanic rocks from the Kastamonu area, northern Turkey. Contrib. Mineral. Petrol. 58, 63–81.

Penaye, J., Kroner, A., Toteu, S.F., Van Schmus, W.R., Doumnang, J.C., 2006. Evolution of the Mayo Kebbi region as reveal by zircon dating: an early (ca. 740 Ma) Pan-African magmatic arc in south-western Chad. J. Afr. Earth Sci. 44, 530–542.

Pham, N.H.T., 2018. Timing and Petrogenesis of Collisional and Post-collisional Rocks of the Guéra Massif, Republic of Chad. MSc Thesis. National Taiwan Normal University, Taipei, p. 167.

Pham, N.H.T., Shellnutt, J.G., Yeh, M.W., Iizuka, Y., 2020. An assessment of the magmatic conditions of Late Neoproterozoic collisional and postcollisional granites from the Guéra Massif, south-central Chad. Front. Earth Sci. 8, 318. https://doi.org/10.3389/feart.2020.00318.

Rieder, M., Cavazzini, G., D'yakonov, Yu.S., Frank Kamenetskii, V.A., Gottardi, G., Guggenheim, S., Koval', P.V., Muller, G., Neiva, A.M.R., Rado Slovich, E.W., Robert, J.L., Sassi, F.P., Takeda, H., Weiss, Z., Wones, D.R., 1999. Nomenclature of the micas. Mineral Mag. 63, 267-79.

Rittmann, A., 1973. Keys for Calculation. Stable Mineral Assemblages of Igneous Rocks. Springer, pp. 88–139.

Rolf, L.R., Write, E.J., 1993. Lead mobilization during tectonic reactivation of the western Baltic Shield. Geochem. Cosmochim. Acta 57, 25552570.

Rudnick, R.L., Gao, S., 2003. Composition of the continental crust. In: Holland, H.D., Turekian, K.K. (Eds.), The Crust Treatise on Geochemistry 3. Elsevier-Pergamon, Oxford, pp. 1–64.

Schwoerer, P., 1962. Carte géologique du Cameroun au 1/500000, coupure de Garoua Est et notice d'explication. Direction des Mines et de la Géologie.

Shand, S.J., 1943. Eruptive Rocks: Their Genesis, Composition, and Classification, with a Chapter on Meteorites. J. Wiley & Sons, Incorporated.

Shellnutt, J.G., Lee, T.-Y., Yang, C.-C., Hu, S.-T., Wu, J.-C., Wang, K.-L., Lo, C.-H., 2015. Late Permian mafic rocks identified within the Doba basin of southern Chad and their relationship to the boundary of the Saharan Metacraton. Geol. Mag. 152 (6), 1073–1084.

Shellnutt, J.G., Pham, N.H.T., Denyszyn, S.W., Yeh, M.-W., Lee, T.-Y., 2017. Timing postcollisional Pan-African Orogeny granitic magmatism within south-central Chad. Precambrian Res. 301, 113–123.

Shellnutt, J.G., Yeh, M.-W., Lee, T.-Y., Iizuka, Y., Pham, N.H.T., Yang, C.-C., 2018. The origin of Late Ediacaran post-collisional granites near the Chad Lineament, Saharan Metacraton, south-central Chad. Lithos 304, 450–467.

Shellnutt, J.G., Yeh, M.-W., Pham, N.H.T., Lee, T.-Y., 2019. Cryptic regional magmatism in the southern saharan metacraton at 580 Ma. Precambrian Res. 332, 105398 https://doi.org/10.1016/j.precamres.2019.105398.

Shellnutt, J.G., Pham, N.H.T., Yeh, M.-W., Lee, T.-Y., 2020. Two series of ediacaran collision-related granites in the Guéra massif, south-Central Chad: tectonomagmatic constraints on the terminal collision of the eastern central African orogenic belt. Precambrian Res. 347, 105823.

Shellnutt, J.G., Yeh, M.-W., Pham, N.H.T., Lee, T.-Y., 2021. Late ediacaran post-collisional magmatism in the Guéra massif, south-Central Chad. Int. Geol. Rev. 64 (8), 1097–1118. https://doi.org/10.1080/00206814.2021.1916783.

Soderlund, U., Patchett, P.J., Vervoort, J.D., Isachsen, C.E., 2004. The 176 Lu decay constant determined by Lu-Hf and U-Pb isotope systematics of Precambrian mafic intrusions. Earth Planet Sci. Lett. 219, 311–324.

Streckeisen, A., 1976. Plutonic rocks: classification and nomenclature recommended by the IVGS sub-commission on the systematic of igneous rocks. Geotimes 18, 26–30.

Sun, S.-S., McDonough, W.F., 1989. Chemical and isotopic systematics of oceanic basalts: implications for mantle composition and processes. In: Saunders, A.D., Norry, M.J. (Eds.), Magmatism in the Ocean Basins, vol. 42. Geological Society of London Special Publication, pp. 313–435.

Sylvester, P.J., 1989. Post-collisional alkaline granites. J. Geol. 97, 261–280.

Tchakounte, J., Eglinger, A., Toteu, S.F., Zeh, A., Nkoumbou, C., Mvondo-Ondoa, J., Penaye, J., deWit, M., Barbey, P., 2017. The Adamawa-Yadé domain, a piece of Archaean crust in the Neoproterozoic Central African Orogenic belt (Bafia area, Cameroon). Precambrian Res. 299, 210–229. https://doi.org/10.1016/j.precamres.2017.07.001.

Toteu, S., 1990. Geochemical characterization of the main petrographical and structural units of Northern Cameroon: implications for Pan-African evolution. J. Afr. Earth Sci. 10 (4), 615–624.

Toteu, S.F., Michard, A., Bertrand, J.M., Rocci, G., 1987. U-Pb dating of Precambrian rocks from northern Cameroon, orogenic evolution and chronology of Pan-African belt of Central Africa. Precambrian Res. 37, 71–87. https://doi.org/10.1016/03019268(87)90040-4.

Toteu, S.F., Van Schumus, W.R., Penaye, J., Michard, A., 2001. New U-Pb and Sm-Nd data from north-Central Cameroon and its bearing on the pre-pan African history of central Africa. Precambrian Res. 108, 45–73.

Toteu, S.F., Penaye, J., Djomani, Y.P., 2004. Geodynamic evolution of the Pan-African belt in central Africa with special reference to Cameroon. Can. J. Earth Sci. 41 (1), 73–85.

Uchida, E., Endo, S., Makino, M., 2007. Relationship between solidification depth of granitic rocks and formation of hydrothermal ore deposits. Resour. Geol. 57, 47–56. https://doi.org/10.1111/j.1751-3928.2006.00004.x.

Vicat, J.-P., Pouclet, A., Nkoumbou, C., Mouangué, A.S., 1997. Le volcanisme fissural néoprotérozoïque des séries du Dja inférieur, de Yokadouma (Cameroun) et de Nola (RCA)- Signification géotectonique. Comptes Rendus Acad. Sci. - Ser. IIA Earth Planet. Sci. 325 (9), 671–677.

Whalen, J.B., Currie, K.L., Chappell, B.W., 1987. A-type granites: geochemical characteristics, discrimination and petrogenesis. Contrib. Mineral. Petrol. 95, 407–419.

Xu, L., Hu, Z.C., Zhang, W., Yang, L., Liu, Y.S., 2015. Gao, S., in situ Nd isotope analyses in geological materials with signal enhancement and non-linear mass dependent fractionation reduction using laser ablation MC-ICP-MS. J. Anal. At. Spectrom. 30 (1), 232–244.

Yang, X.-M., Lentz, D.R., Chi, G., 2021. Ferric-ferrous iron oxide ratios: effect on crystallization pressure of granites estimated by Qtz-geobarometry. Lithos 380, 105920.

Yomeun, B.S., Wang, W., Tchouankoue, J.P., Kamani, M.S.K., Ndonfack, K.I.A., Huang, S.-F., Basua, E.A.A., Lu, G.-M., Xue, E.-K., 2022a. Petrogenesis and tectonic implication of neoproterozoic I-type granitoids and orthogneisses in the Goa-mandja area, central african fold belt (Cameroon). Lithos 420, 106700.

Yomeun, B.S., Wang, W., Kamani, M.S.K., Tchouankoue, J.P., Jiang, Y.-D., Huang, S.-F., Ndonfack, K.I.A., Xue, E.-K., Lu, G.-M., Basua, E.A.A., 2022b. Geochronology, geochemistry and Sr-Nd, Hf-O isotope systematics of the linte massif, Adamawa-Yade domain, Cameroon: implications on the evolution of the central african fold belt. Precambrian Res. 375, 106675.

Zhang, X.O., Cawood, P.A., Wilde, S.A., Liu, R., Song, H., Li, W., Snee, L.W., 2003. Geology and timing of mineralization at the Cangshang gold deposit, north-western Jiaodong Peninsula, China. Miner. Deposita 38 (2), 141–153.

Zhang, L., Chen, Z.-Y., Tian, Z.-J., Huang, G.-L., 2016. The application of electron microprobe dating method on uranium minerals in Changjiang granite, northern Guangdong. Rock Miner. Anal. 35 (1), 98–107.

Zong, K., Klemd, R., Yuan, Y., He, Z., Guo, J., Shi, X., Liu, Y., Hu, Z., Zhang, Z., 2017. The assembly of Rodinia: the correlation of early Neoproterozoic (ca. 900 Ma) high-grade metamorphism and continental arc formation in the southern Beishan Orogen, southern Central Asian Orogenic Belt (CAOB). Precambrian Res. 290, 32–48.